ROLE OF SOLVENT ON FABRICATION OF ESSENTIAL AMINO-ACID BASED NANOPARTICLES DIRECTED FOR PHOTOTHERMAL THERAPY

M.Sc. Thesis

By

VIBHA CHOUDHARY

DEPARTMENT OF BIOSCIENCES AND BIOMEDICAL ENGINEERING

INDIAN INSTITUTE OF TECHNOLOGY INDORE

MAY 2024

ROLE OF SOLVENT ON FABRICATION OF ESSENTIAL AMINO-ACID BASED NANOPARTICLES DIRECTED FOR PHOTOTHERMAL THERAPY

M.Sc. Thesis

By
VIBHA CHOUDHARY
2203171021

DEPARTMENT OF BIOSCIENCES AND BIOMEDICAL ENGINEERING
INDIAN INSTITUTE OF TECHNOLOGY INDORE
MAY 2024

ROLE OF SOLVENT ON FABRICATION OF ESSENTIAL AMINO-ACID BASED NANOPARTICLES DIRECTED FOR PHOTOTHERMAL THERAPY

A THESIS

Submitted in partial fulfillment of the
requirements for the award of the degree
of
Master of Science

by

VIBHA CHOUDHARY

DEPARTMENT OF BIOSCIENCES AND BIOMEDICAL ENGINEERING
INDIAN INSTITUTE OF TECHNOLOGY INDORE
MAY 2024

INDIAN INSTITUTE OF TECHNOLOGY INDORE

CANDIDATE'S DECLARATION

I hereby certify that the work which is being presented in the thesis entitled **ROLE OF SOLVENT ON FABRICATION OF ESSENTIAL AMINO ACID BASED NANOPARTICLES DIRECTED FOR PHOTOTHERMAL THERAPY** in the partial fulfillment of the requirements for the award of the degree of **MASTER OF SCIENCE** and submitted in the **DEPARTMENT OF BIOSCIENCES AND BIOMEDICAL ENGINEERING, Indian Institute of Technology Indore**, is an authentic record of my own work carried out during the time period from July 2022 to May 2024 under the supervision of Dr. Sharad Gupta, Associate Professor.

The matter presented in this thesis has not been submitted by me for the award of any other degree of this or any other institute.

Vibha 24/05/2024
Signature of the student with date
(VIBHA CHOUDHARY)

This is to certify that the above statement made by the candidate is correct to the best of my knowledge.

Sharad Gupta 24 May 2024
Signature of the Supervisor of
M.Sc. thesis (with date)
Dr. SHARAD GUPTA

VIBHA CHOUDHARY has successfully given her M.Sc. Oral Examination held on **10 MAY 2024**.

Sharad Gupta 24 May 2024
Signature of Supervisor of MSc thesis
Date:

P.V. Kodgire
Convener, DPGC
Date: 24/05/24

---

i

ACKNOWLEDGEMENTS

Firstly, I would like to express my sincere thanks to my wonderful parents and family members for their continuous support throughout this journey.

I would like to thank my supervisor **Dr. Sharad Gupta**, whose unwavering support has been instrumental in the completion of this thesis. His priceless advice and unwavering support during the research process have left me incredibly grateful.

I want to convey my sincere gratitude to **Miss Anusha Srivastava** (Ph.D. scholar), for providing me with a solid grounding in the field of research. I sincerely appreciate all of her help and inspiration to do this task despite her incredibly hectic schedule.

This work is carried out at the Indian Institute of Technology Indore. I, duly acknowledge the infrastructure and research facility provided by the Department of Biosciences and Biomedical Engineering (BSBE) and Sophisticated Instrument Centre (SIC), Indian Institute of Technology Indore.

I would duly acknowledge **Prof. Amit Kumar** (Head, Department of Biosciences and Biomedical Engineering), **Prof. Prashant Kodgire** (DPGC), **Dr. Parimal Kar** (Course coordinator) and all the BSBE faculty members for their insightful suggestions, encouragement and moral support.

I would like to thank **Dr. Abhijeet Joshi** for his help in the UV-visible spectroscopy experiment and his student **Badri Narayana Sahoo** for his patience and valuable time.

I would like to thank my senior **Priyanka Payal** and my lab mates Moumita Pal and Neeraj Sati for their help and support.

I would like to extend my sincere thanks to Arif Patel and Gaurav Singh for their kind nature and help regarding instruments as well as official works. I would also like to thank academic authorities and library authorities of IIT Indore, and other technical and non-technical staff for their constant support whenever required.

I would like to express my sincere thanks to my sister Abha Choudhary for immeasurable support with the deepest sense of love and to my ever-smiling friends Kh. Humendro Singh, Simran Rana, Diksha Madavi, Shivani Vaja and Bidisha Choudhary with whom this journey was joyful.

This thesis is dedicated to

My beloved family

&

My senior Anusha Srivastava

ABSTRACT

Nanoparticle-mediated targeted drug delivery has revolutionized nano-therapeutics. It ensures improved biodistribution, bioavailability and drug accumulation in targeted diseased locations inside the body. The right concentration of the drug and stability of the carrier are the major challenges for efficient targeted drug delivery. In this study, we have synthesized indocyanine green (ICG) loaded Poly-L-Lysine (PLL) nanoparticles by the two-step self-assembly process. Different solvents; phosphate-buffered saline (PBS), deionized water and Milli-Q water have been used to identify how the solvent selection affects the stability and encapsulation efficiency of the nanoparticles. The effect of solvent interaction on nanoparticles morphology, stability, and encapsulation efficiency was investigated using scanning electron microscopy (SEM), UV-visible spectroscopy, and fluorescence spectroscopy. The results demonstrated maximum loading, stability and nanoparticle formation in case of PBS buffer followed by deionized water and Milli-Q water respectively. The ICG-loaded PLL nanoparticles lying in the near-infrared therapeutic window were then tested for their cytotoxicity and photothermal efficiency.

TABLE OF CONTENT

Abstract	**v**
List of figures	**ix**
List of tables	**xii**
Abbreviations	**xiii**
Chapter 1: Introduction	**1**
1.1 Cancer Statistics	1
1.2 Overview of cancer	2
1.3 Types of cancer treatment	2
1.4 Limitations of the cancer treatment	3
1.5 Photothermal therapy	4
1.6 Nanoparticle-mediated photothermal therapy	4
1.7 Photothermal agents (PTA)/Contrast agents	5
1.8 Different types of nanocarriers	6
Chapter 2: Literature review	**7**
2.1 Background study	7
2.2 ICG as a photothermal agent	7
2.3 Poly-L-lysine based nanoparticle	9
2.4 Near-infrared imaging	11
2.5 Photothermal therapy for cancer treatment	11
Chapter 3: Objectives	**14**
3.1 Objective 1	14
3.2 Objective 2	14
3.3 Objective 3	14
Chapter 4: Materials and Methods	**15**
4.1 Materials	15
4.2 Methods	15
4.2.1 Preparation of stock solutions	15
4.2.1.1 Poly-L-lysine	15

4.2.1.2 ICG 15
4.2.1.3 PBS 16
4.2.1.4 Complete DMEM media 16
4.2.1.5 MTT 16
4.2.2 Fabrication of PLL-ICG NPs 16
4.2.3 Preparation of PLL-ICG NPs in different solution 17
4.2.4 Optical characterization 17
4.2.4.1 UV-visible spectroscopy 17
4.2.4.2 Fluorescence spectroscopy 19
4.2.4.3 Circular dichroism spectroscopy 20
4.2.4.4 Morphological characterization 20
4.2.4.5 Estimation of encapsulation efficiency of NPs 21
4.2.4.6 In-vitro release study 21
4.2.4.7 Measurement of temperature elevation of NPs 22
4.2.4.8 Cell culture 23
4.2.4.9 Cell viability and cellular uptake study 23
4.2.4.10 Assessment of cell viability after laser treatment 24
4.2.4.11 ROS generation assay 24
4.2.4.12 Live/dead assay 25

Chapter 5: Results and Discussions 27
5.1 Spectroscopic analysis 27
5.2 Morphological characterization 30
5.3 %EE Calculation 31
5.4 In-vitro release study 32
5.5 PTT efficiency of bare NPs 33
5.6 Cytotoxicity assay 35
5.7 Cellular uptake study 37
5.8 MTT assay after laser treatment 39
5.9 Live/dead assay 40
5.10 ROS generation assay 42

Chapter 6: Conclusion and Future Scope 44

6.1 Conclusion 44
6.2 Future scope 45

References **46**

LIST OF FIGURES

Chapter 1. Introduction

Figure 1.1 Cancer Statistics in India 2

Figure 1.2 Different types of cancer treatment 3

Figure 1.3 Overview of nanocarrier-mediated photothermal therapy 5

Chapter 2. Literature review

Figure 2.1 Molecular structure of ICG 8

Figure 2.2 Molecular structure PLL 10

Chapter 3. Objectives

Figure 3.1 Overview of the study 14

Chapter 4. Materials and Methods

Figure 4.1 Two-step self–assembly method for the production of PLL NPs 16

Figure 4.2 Pictorial diagram of preparation of PLL-ICG NPs 17

Figure 4.3 Different solvents used for the preparation of PLL NPs 17

Figure 4.4 Range of EM wave 18

Figure 4.5 Predicting protein structure using CD spectroscopy 20

Figure 4.6 Mechanism of DCFDA in ROS generation assay 25

Chapter 5. Results and discussions

Figure 5.1 Absorption spectra of free ICG & PLL-ICG NPs 28

Figure 5.2 Emission spectra of free ICG and PLL-ICG NPs 29

Figure 5.3 CD spectra of PLL, PLL NP and PLL-ICG NPs 30

Figure 5.4 SEM analysis of PLL-ICG nanoparticles morphology 31

Figure 5.5 Calibration curve of free indocyanine green (ICG) in dimethyl sulfoxide (DMSO) 32

Figure 5.6 Cumulative percentage ICG release from PLL NPs in different solvents 33

Figure 5.7 Photothermal efficiency curve of PLL-ICG NPs 34

Figure 5.8 Infrared thermal images of PLL-ICG NPs 35

Figure 5.9 PTT efficiency curve of PLL-ICG NPs prepared in PBS 35

Figure 5.10 In-vitro cytotoxicity analysis of PLL NPs, 36

free ICG and PLL-ICG NPs

Figure 5.11 Cellular uptake of free ICG and PLL-ICG NPs prepared in PBS 38

Figure 5.12 Cellular uptake of PLL-ICG NPs prepared in MQ, DI and PBS 38

Figure 5.13 MTT assay of MCF-7 post laser irradiation 39

Figure 5.14 MCF-7 cells, costained with Calcein and PI 40

Figure 5.15 Fluorescence image of 3D-cell model of MCF-7 after laser irradiation 41

Figure 5.16 Fluorescence image of 3D-cell model of MCF-7 after treated with PLL-ICG NPs followed by laser irradiation 42

Figure 5.17 Cells stained with DCFDA dye 43

LIST OF TABLES

Chapter 4. Results and Discussions

Table 1. Concentration and EE% of PLL-ICG NPs in their respective solvents 32

Table 2. Cumulative % release of ICG at different time points 33

ABBREVIATION

PLL	Poly-L-lysine
PTT	Photothermal Therapy
PTA	Photothermal Agents
ICG	Indocyanine Green
NPs	Nanoparticles
MQ	Milli- Q Water
DI	Deionized Water
PBS	Phosphate Buffered Saline
NIR	Near Infrared
UV	Ultra Violet
CD	Circular Dichroism
WHO	World Health Organization
FDA	Food and Drug Administration
DMEM	Dulbecco's Modified Eagle Medium
DMSO	Dimethyl Sulfoxide
FBS	Fetal Bovine Serum
DAPI	4',6-diamidino-2-phenylindole
FE-SEM	Field Emission Scanning Electron Microscopy
DLS	Dynamic Light Scattering
MCF-7	Michigan Cancer Foundation - 7
EPR	Enhanced Permeability and Retention Effect

Chapter - 1

Introduction

1.1 Cancer statistics

Cancer is the deadliest disease in the world. There exists documented evidence that cancer-related deaths are rising globally today. By 2030, the WHO predicts that there will be more than 13.2 million cancer-related deaths and about 21.4 million new instances of the disease [1]. Cancer poses a growing health concern in India, affecting individuals from various socio-economic backgrounds and regions of the country. The incidence of cancer is steadily rising, with a higher number of cases being recorded annually [3]. In 2022, it was estimated that India would see around 1,461,427 new cancer cases, equating to a crude incidence rate of 100.4 per 100,000 people. Approximately one out of every nine individuals in India is predicted to receive a cancer diagnosis at some point in their lives. Notably, lung cancer was the most common among males, while breast cancer topped the list for females [4]. Looking ahead, there's an anticipated 12.8% increase in cancer incidence by 2025 compared to 2020. Breast cancer stands as the predominant form of cancer among women in India, representing 14% of female cancer cases. On average one woman receives a breast cancer diagnosis every four minutes in India. The incidence of breast cancer is escalating across both rural and urban areas of the country [5]. The undeniable truth is that breast cancer has surpassed cervical cancer to become the most prevalent type of cancer in India. In major cities such as Mumbai, Delhi, Bengaluru, Bhopal, Kolkata, Chennai, and Ahmedabad, breast cancer constitutes between 25% to 32% of all cases of female cancer, accounting for over a quarter of all female cancer diagnoses [6].

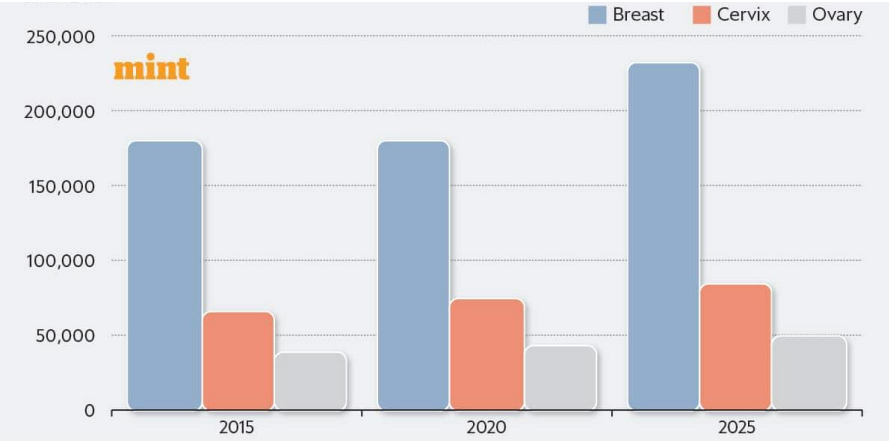

Figure 1.1. Cancer statistics in India: Estimated trend of cancer cases in females in India in 2015, 2020 and 2025 [2].

1.2 Overview of cancer

Cancer is an abnormal proliferation of cells without differentiation and apoptosis. Cancer cells typically display several abnormal properties as compared to normal cells. Cancer cells do not show contact inhibition, unlike normal cells. Another striking difference displayed by cancer cells is illustrated by the phenomenon of contact inhibition. Most of the cancer cells fail to differentiate and do not show apoptosis. The most common reason for cancer is defective or damaged genetic material. Any certain changes in DNA sequence or alteration in repair mechanism during DNA replication cause the change of normal cells into cancer cells. Additionally, it is observed that cells displaying defective DNA and altered repair processes demonstrate chemoresistance traits [6]. Due to these diversities in cancer biology, it is difficult to treat the cancer.

1.3 Different types of cancer treatment

The treatment of cancer involves a multifaceted approach. Treatment options for cancer depend on factors such as the type and stage of cancer, as well as the patient's overall health and preferences. Common treatment modalities include surgery, chemotherapy, radiation therapy, targeted therapy, immunotherapy, hormone therapy, and stem cell

transplant. Often, a combination of these treatments is used to achieve the best possible outcome [7].

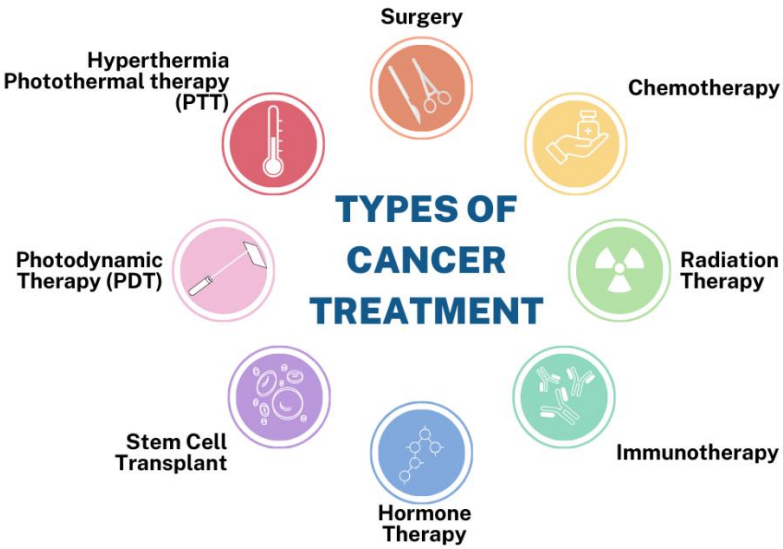

Figure 1.2. Different types of therapies which is used for the treatment of the cancer disease.

1.4 Limitations of the cancer treatment

Conventional methods like surgery, radiation therapy, and chemotherapy, as well as combination approaches, come with several limitations. Surgery, while aiming to eradicate cancer cells, may not always remove all of them, potentially leading to significant complications. Moreover, it's often employed to excise numerous tumors located near vital structures. Similarly, radiation therapy is associated with various adverse effects such as fatigue, headache, and memory problems, causing considerable distress to patients [8]. One of the main therapeutic modalities for the treatment of cancer is chemotherapy, which may be used either alone or in conjunction with other types of therapy. The conventional chemotherapy used for cancer treatment comes with some major shortcomings like less water solubility and selectivity, drug resistance. Chemotherapy tends to damage both cancerous and non-cancerous cells as they are not target-specific [9]. Considering all these limitations of existing therapies, we need to employ a new modality to treat tumors.

1.5 Photothermal therapy

Photothermal therapy is a process in which, a variety of photothermal agents are used to absorb optical radiation and then transform the absorbed energy to heat. When these photothermal agents (PTA) are incubated with biological samples such as cells, this heat energy causes the rise in temperature in targeted cells, due to the localized temperature rise cells get damaged [10]. Hyperthermia/ Photothermal therapy has drawn a lot of attention from research groups because it causes the killing of cells by protein denaturation or cellular membrane rupture. It has gained popularity because it shows minimal invasion to the neighbouring cells, high efficacy, less toxicity, excellent targeting and good acceptance by the majority of tumors [10]. To increase the bioavailability and target cancer cells the photothermal agents are also being encapsulated within nanoparticles.

1.6 Photothermal agents (PTA)/ contrast agents

Photothermal agents are substances or materials that have the ability to absorb light energy and convert it into heat. In the context of photothermal therapy (PTT), these agents are utilized to selectively generate heat within target tissues, typically tumors, for therapeutic purposes. When exposed to light of specific wavelengths, photothermal agents undergo a process known as photothermal conversion, where absorbed light energy is converted into heat. This localized heating effect can be exploited to destroy cancer cells or disrupt tumor tissues [12]. An ideal photothermal agent should possess a high stability at the treatment wavelength, good biocompatibility that includes minimal dark toxicity outside of the light-exposed tissue. Generally, photothermal agents are divided into the following types: (i) organic dyes, e.g. indocyanine green and heptamethine cyanine, (ii) nanoparticles e.g. gold nanorods and gold nanoshells, (iii) carbon nanotubes and graphene nanosheets, (iv) upconversion nanoparticles.

1.7 Different types of nanocarriers

Nano-encapsulation of the PTAs is beneficial in numerous ways. It helps to improve the shelf life and optical stability of the light sensitive agent and controls the release of PTAs. Nanobiotechnology has significantly advanced site-specific drug delivery applications. The nanoencapsulation of these PTAs has also improved their molecule half-life, increasing effective concentrations at specific locations, and reducing side effects. In recent years, a diverse array of nanoparticles has been developed as drug carriers, including metal nanoparticles (NPs), polymer-based NPs, liposomes, and more. These nanoparticles offer unique advantages such as tunable size, surface modification for targeting specific cells or tissues, and controlled release of therapeutic payloads [13]. Metal nanoparticles, such as gold or silver NPs, possess excellent biocompatibility and can be functionalized with targeting ligands for precise drug delivery [14]. Polymer-based nanoparticles provide versatility in encapsulating various types of drugs and controlling their release kinetics. Liposomes offer a lipid bilayer structure that mimics cell membranes, facilitating efficient drug delivery and minimizing immunogenicity. Overall, the convergence of nanotechnology and biomedicine has paved the way for the development of advanced drug delivery systems with enhanced efficacy and reduced adverse effects.

In this thesis we present the photothermal application of an FDA approved near infrared chromophore Indocyanine Green (ICG) within polymeric nanoparticles. The nanoencapsulated ICG has shown superior photothermal efficiency than free ICG and might be used for the photothermal therapy of tumors.

1.8 Nanoparticles mediated photothermal therapy

Despite the significant progress made in photothermal therapy (PTT) for treating cancer, its efficacy has been hindered when employing laser illumination to PTAs. This is primarily due to and their limited accumulation in tumor tissues, and the development of heat resistance in certain types of cancer [10]. Using nanomaterials for the delivery of PTT agents provides enhanced therapeutic benefits with reduced side effects [11]. This improvement stems from the increased efficiency of converting light into heat, enhanced accumulation of the PTT agent within tumor tissues, and the potential for synergistic effects when combined with other therapies.

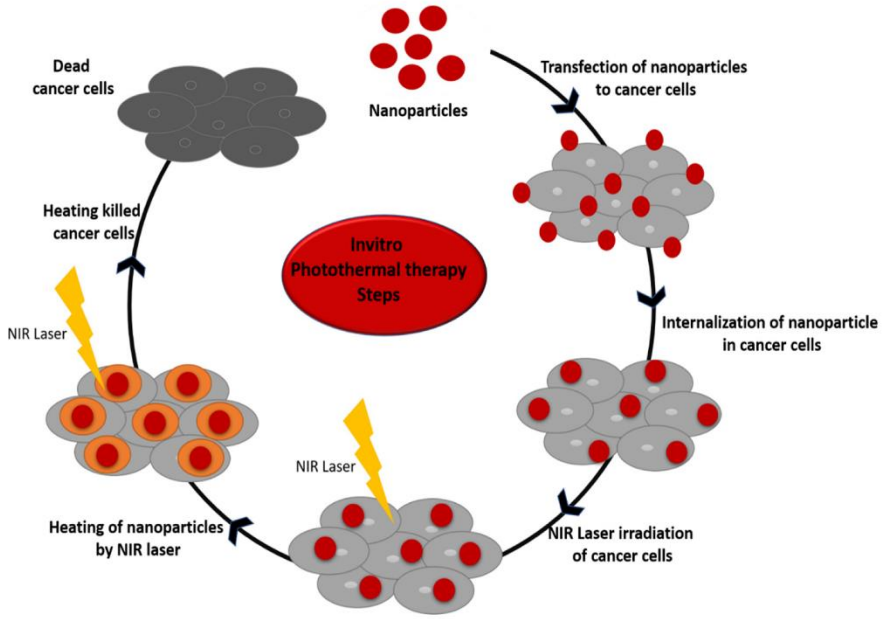

Figure 1.3. Overview of nanocarrier-mediated photothermal therapy

Chapter – 2
Literature Review

2.1 Background study

Photothermal therapy using biodegradable nanoparticles holds significant promise for enhancing anticancer therapy. These NPs, typically made of materials such as niosome, biopolymer or liposome, can be designed as a vehicle to deliver the contrast agent and selectively accumulate in tumor tissues through active or passive targeting mechanisms. Once localized within the tumor, these nanoparticle encapsulated contrast agents can be activated using near-infrared (NIR) light, which penetrates deeply into tissue without causing damage to surrounding healthy cells [14]. When exposed to NIR light, the contrast agents convert light energy into heat, leading to localized hyperthermia within the tumor. This hyperthermia induces various biological effects, including tumor cell death, destruction of tumor vasculature, and activation of the immune system against cancer cells. Importantly, the biodegradable nature of these nanoparticles ensures that they can be metabolized and cleared from the body after therapy, minimizing potential long-term toxicity [15]. Overall, photothermal therapy employing biodegradable nanoparticles represents a promising approach for enhancing the efficacy and safety of cancer treatment. Continued research efforts aimed at optimizing nanoparticle design, improving tumor targeting, and evaluating clinical outcomes are essential for realizing the full potential of this innovative therapeutic strategy.

2.2 ICG as a photothermal agent

ICG is an FDA-approved NIR fluorescent dye, used in several biomedical applications. It is comprised of two sulphonate groups, with a molecular weight of 774.94 Daltons.
The absorption and emission spectra of ICG are primarily situated in the near-infrared range. ICG predominantly absorbs light between 600

nm and 900 nm, while its fluorescence emission occurs between 750 nm and 950 nm. The substantial overlap between the absorption and fluorescence spectra results in significant reabsorption of emitted fluorescence by ICG molecules themselves [16]. Additionally, the fluorescence spectrum of ICG is notably broad. For medical applications based on absorption, the maximum absorption at approx. 800 nm is important.

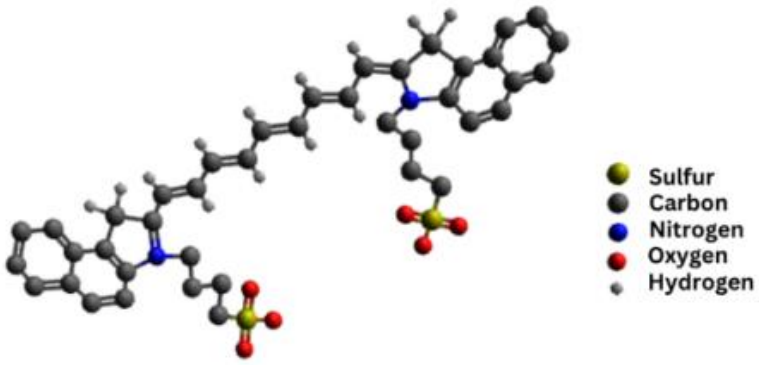

Figure 2.1. Molecular structure of ICG.

ICG tends to form aggregation, due to its tendency to possess strong intramolecular Van der Waals forces. This aggregation property depends on various factors like solvent, pH, temperature and concentration. In aqueous solution, monomers are prominent at lower concentration, however, at higher concentrations dimers and oligomers are prominent. In comparison to monomeric species, the aggregated form exhibit distinct changes in the NIR absorption band. Higher order of aggregates in ICG, exhibit a hypsochromic shift (towards the blue) compared to the monomer band termed as H-aggregates and bathochromic shift (towards the red wavelength) compared to the monomer band of ICG denoted as J-aggregates. The H-aggregates are stacked in a plane-to-plane manner. While J-aggregates were made up of parallel arrangements of the ICG molecules (end-to-end or head-to-tail arrangement) [17] ICG has been utilized as a photothermal agent in various biomedical applications. Although, primarily known

as a near-infrared (NIR) fluorescent dye used in medical imaging, ICG has gained attention for its photothermal properties. In PTT, ICG is administered to the patient, where it accumulates preferentially in tumor tissues due to the enhanced permeability and retention (EPR) effect. When exposed to NIR light at wavelengths that match its absorption spectrum, ICG molecules absorb the light energy, leading to localized heating and subsequent thermal ablation of the tumor cells. This targeted approach minimizes damage to surrounding healthy tissues, particularly in photothermal therapy (PTT) of cancer cells. The use of ICG as a photothermal agent offers several advantages, including its biocompatibility, minimal toxicity, and efficient conversion of NIR light into heat [18].

When ICG is administered in its free form, it can exhibit off-target distribution within the body, leading to suboptimal imaging outcomes. This can be particularly problematic when attempting to visualize specific tissues or organs accurately. In aqueous solutions, ICG tends to aggregate in a concentration-dependent manner. This aggregation can affect the dye's optical properties. ICG is susceptible to photodegradation, especially under prolonged exposure to light. This can lead to a decrease in absorbance and fluorescence efficiency over time, reducing the effectiveness of ICG-based imaging techniques [19]. These limitations hinder the widespread use of ICG as a near-infrared (NIR) active exogenous contrast agent for bioimaging, especially for applications requiring deep tissue imaging with high spatial resolution and sensitivity. To address these challenges and maximize the utility of ICG in bioimaging and photothermal therapy, it can encapsulate within nanoparticles.

2.3 Nanoencapsulation of ICG within Poly-L-lysine based nanoparticles

There are various nanocarriers for site-specific drug delivery, such as metal nanoparticles, liposomes, and polymer-based nanoparticles. This advancement has enhanced the effectiveness of diagnosing and treating

diseases. However, many of these nanoparticles face several challenges, including limited biocompatibility, non-biodegradability, and potential cytotoxicity over both short and long durations. Consequently, there is a growing interest in developing nanocarriers using biomacromolecules like lipids, proteins, and amino acids to deliver drugs and contrast agents. In this study, we have planned to use biocompatible and biodegradable PLL and salt crosslinked nanoparticles to encapsulate the ICG for photothermal therapy. Poly-L-lysine is the polymer of positively charged essential amino acid lysine [16]. It is often used in biological research and medical applications. Poly-L-lysine is known for its ability to enhance the adhesion of cells to surfaces [18]. It is commonly used to coat cell culture dishes, slides, and other surfaces to promote cell attachment and growth in vitro. This property makes it valuable in various laboratory techniques, such as cell culture, immunocytochemistry, and tissue engineering. Additionally, poly-L-lysine can also be used as a drug delivery system in various medical applications.

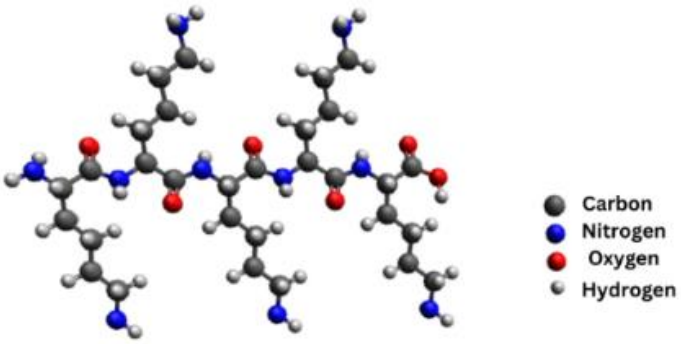

Figure 2.2. Molecular structure of Poly-L-lysine.

PLL based NPs have been utilized in various biomedical and pharmaceutical applications due to their unique properties and versatility. PLL NPs are biocompatible and non-toxic, making it suitable for biomedical applications [19]. PLL can be used to encapsulate drugs, genes, or other therapeutic agents and deliver them to target cells or tissues. The surface of poly-L-lysine nanoparticles can

be modified with targeting ligands or functional groups to enhance specific cell targeting and internalization.

2.4 Near-infrared imaging

Near-infrared (NIR) imaging is revolutionizing biomedical research and clinical diagnostics with its unique capabilities. By exploiting light in the near-infrared spectrum, NIR imaging enables non-invasive visualization of deep tissues and structures within biological samples. Unlike visible light, NIR light penetrates tissues with minimal scattering and absorption, allowing for clear imaging of internal organs, tumors, and physiological processes. This deeper tissue penetration, coupled with reduced autofluorescence, enhances the sensitivity and specificity of NIR imaging, facilitating the detection of molecular targets with high precision. Furthermore, NIR imaging supports multiplexing, enabling simultaneous visualization of multiple targets within the same sample, thus providing valuable insights into complex biological interactions. In clinical settings, NIR imaging holds promise for intraoperative navigation, tumor detection, and assessment of tissue perfusion, contributing to improved patient outcomes and personalized medicine [21]. Overall, NIR imaging represents a powerful and versatile tool for advancing our understanding of biology and enhancing diagnostic and therapeutic strategies in healthcare. In this study, we have shown that in-vitro cellular uptake of PLL-ICG NPs incubated cells had significantly higher NIR fluorescence emission in comparison to the free-form of ICG. In this study we have used NIR contrast agent and NIR laser for efficient photothermal therapy.

2.5 Photothermal therapy for cancer treatment

Hyperthermia has got great attention because it leads to death by protein denaturation or break of the cellular membrane and afterward results in tumor shrinkage because of the removal of cancer cells by macrophages, which get more benefits over conventional cancer therapies including minimal invasion, easy to perform, and possibilities to treat situated tumors in essential regions where surgery is not

available [22]. Yet, to treat basic tumors, the activation energy source need not only adequately penetrate healthy tissues, but also efficiently kill tumors without invasion to healthy tissues. Therefore, particular energy absorbing nanoagents are serious, which are situated in particular tumors to absorb energy and ease of thermal therapy. Nowadays, some heating sources such as microwaves, laser light and centered ultrasound are engaged in thermal cancer treatment.

PTT is another treatment that increases interest in scientific community rather than conventional therapy. Because it has therapeutic efficacy, low toxicity, high targeting, good acceptability it becomes more popular. It is also an invasive technique. Photothermal therapy has drawn appreciable observation because of its excellent tumor tissue clear out ability and almost no harm to simple tissues [23]. In Photothermal therapy many photothermal agents are used that absorbs the radiation near in the spectral region and convert the absorbed energy light into heat through a non-radiative procedure without oxygen consumption. Photothermal method is mostly utilized nanomaterials because shows more absorption in the NIR region of the electromagnetic spectrum. Nanomaterials increase permeability and retention effect. Photothermal agents inside tumors result from energy transfer from light to heat, which rises temperature to destroy tumor cells.

Many organic light absorbers in tissue including water, oxyhemoglobin, hemoglobin, and melanin can convert light to heat, which shows in increase in the temperature cause harm in both tumors and healthy tissues. Still, the near-infrared light persuade least Photothermal temperature increase in both tumors and tissues, as the absorption of biological tissues consisting of blood and water is minimal in a NIR region 700 nm to 900 nm [24]. Therefore, many photothermal nanoparticles that can absorb NIR light to affect the particular tumor with negligible damage to the nearby healthy tissues by conversing NIR light to heat have been developed and systematically investigated, which possess high Photothermal

conversion efficiency, and strong absorbance and good photostability in the NIR region [25].

In this study, we have encapsulated ICG within a homopolymer of lysine and salt crosslinked nanoparticles for their photothermal applications. These nanoparticles have shown better uptake of ICG in comparison to its free form and have better therapeutic outcomes. Also, the purpose of this research is to investigate how different solvents affect the functional and morphological properties of the ICG-loaded PLL NPs. The major focus of this research is to evaluate the photothermal properties of the PLL-ICG NPs and perform photothermal therapy in cancer cells.

Chapter – 3

Objectives

The main objective of this study is to fabricate the PLL-ICG NPs and to check how different solvents affect the functional and morphological nanoparticles. Further to check the biocompatibility and photothermal efficiency of these nanoparticles for cancer treatment.

1. Formulation of ICG (Indocyanine Green) loaded poly-l-lysine (PLL) nanoparticles through two step self-assembly process and its morphological and functional characterization.
2. Role of MQ water, DI water and PBS on the stability, morphology, size, encapsulation efficiency and photothermal efficacy of PLL-ICG NPs.
3. Photothermal efficiency of bare PLL-ICG NPs and its in-vitro application with cells (cytotoxicity assays, bio-imaging and photothermal therapy).

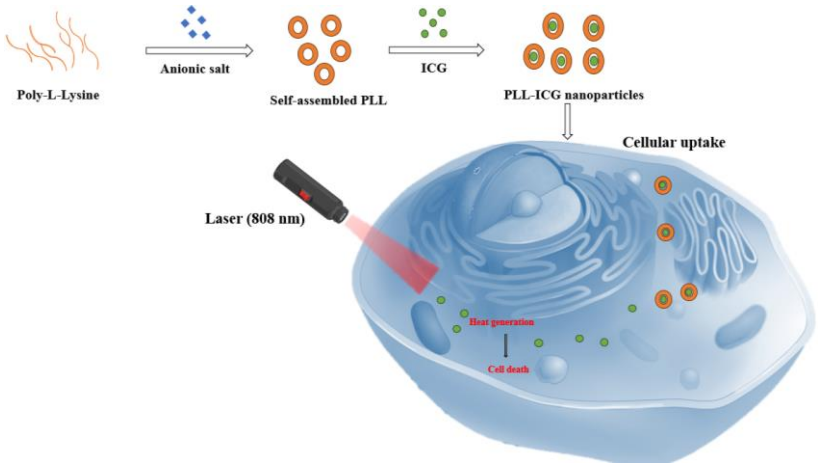

Figure 3.2. Illustration of two-step self-assembly of ICG encapsulated PLL nanoparticles, transfer of nanoparticles into the cancer cell, release of ICG from PLL nanoparticle in the cell, photothermal damage of cancer cell by laser (808 nm).

Chapter – 4
Material and Methods

4.1 Materials

Poly-L-Lysine, abbreviated as PLL, (~574 lysine unit, one HBr per lysine unit, Molecular weight=120 KDa) was purchased from Polysciences (Warrington, PA, USA). Indocyanine green (ICG) and sodium phosphate dibasic heptahydrate were procured from Sigma Aldrich (St. Louis, MO, USA). Trisodium citrate dihydrate was purchased from Merck (Darmstadt, Germany). PBS buffer reagents which include, sodium chloride (NaCl), potassium chloride (KCl), disodium hydrogen phosphate (Na_2HPO_4), and potassium dihydrogen phosphate (KH_2PO_4) were purchased from Thomas Baker (Mumbai). All of the stock solutions were prepared in Milli-Q water (Sartorius, 18 MΩ) and stored at 4°C. Dimethyl sulfoxide was purchased from MP Biomedicals, LLC. MCF-7 cell lines, Fetal Bovine Serum (FBS), Dulbecco's Modified Eagle Medium (DMEM), 0.25% trypsin-1 mM ethylenediaminetetraacetic acid (EDTA), penicillin-streptomycin, and 2.5% trypsin without phenol red were purchased from Gibco (Thermo Fisher Scientific Inc., India). Colorimetric assay (MTT, (3-(4, 5-dimethylthiazol-2-yl)-2, 5-diphenyltetrazolium bromide)) was procured from Himedia Chemicals (India).

4.2 Methods

4.2.1 Preparation of stock solution

4.2.1.1 Poly-L-Lysine

The concentration of stock solution of PLL is 3 mg/mL. It was prepared by adding PLL flakes in MQ water and stored at 0 ˚C.

4.2.1.2 Indocyanine green

The stock solution of ICG, with a concentration of 645 µM, was prepared by dissolving ICG powder in MQ water and then stored at -80 ˚C in a dark environment.

4.2.1.3 Phosphate buffer saline solution

The stock solution of 1X PBS was created by dissolving 8 grams of NaCl, 0.2 grams of KCl, 1.44 grams of Na_2HPO_4, and 0.24 grams of KH_2PO_4 in water. The pH was adjusted to 7.4 using either NaOH or HCl. This stock solution was then stored at 4°C.

4.2.1.4 Complete DMEM media

To The nutrient enriched DMEM media for culturing cells was prepared by combining 45 mL DMEM, 5 mL (10% V/V) fetal bovine serum, and 500 µL (1% V/V) of L-glutamine and penicillin-streptomycin each.

4.2.1.5 MTT solution

5 mg/mL MTT stock solution was made by dissolving 5 mg of MTT powder to 1 mL of 1X PBS (pH= 7.4). Further dilutions were made in serum free media.

4.2.2 Fabrication of PLL-ICG NPs

PLL (20 µL) was taken in a 1.5 mL MCT from stock PLL stock solution (3 mg/mL)1. 13.2 µL Trisodium citrate dihydrate (0.01 M) and 2 µL sodium phosphate dibasic heptahydrate (0.01 M) was added in the PLL solution and mixed it gently. The solution of PLL and salt became turbid because of initiation of self-assembly of nanoparticles. After 10 seconds, 200 µL ICG solution was added into the MCT which consisted PLL and salt solution. After that 1X PBS was added to make up final volume as 1 mL. The sample was aged for approximately 40 minutes at 4˚C. After incubation, differential centrifugation (3500 rpm for 5 minutes and 7500 rpm for 20 minutes) was done to pellet down the monodisperse ICG loaded PLL NPs.

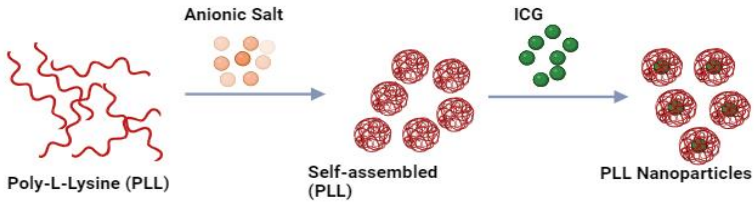

Figure 4.1. Two-step self–assembly method for the production of PLL-ICG nanoparticles.

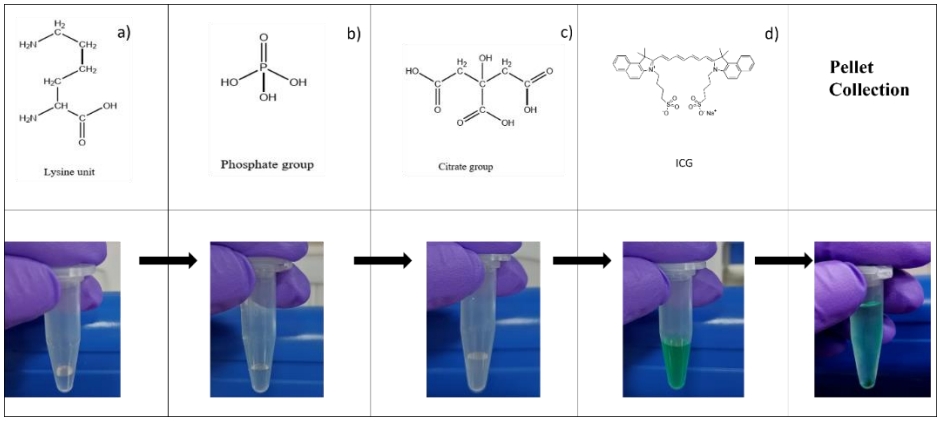

Figure 4.2. The creation of poly-l-lysine (PLL) nanoparticles is depicted in a pictorial diagram. (a) Displaying a 1.5 mL Eppendorf tube filled with a clear PLL solution. (b) After the addition of salts, PLL solution became turbid. (c) Addition of 200 µL of ICG. (d) Image of the pellet after differential centrifugation.

4.2.3 Preparation of PLL-ICG NPs in different solvents

To study how different solvent affect the structure and loading efficiency of PLL NPs, three different solvents PBS buffer, DI water and MQ water has been used. In the above steps, different solvent were added after adding the ICG solution.

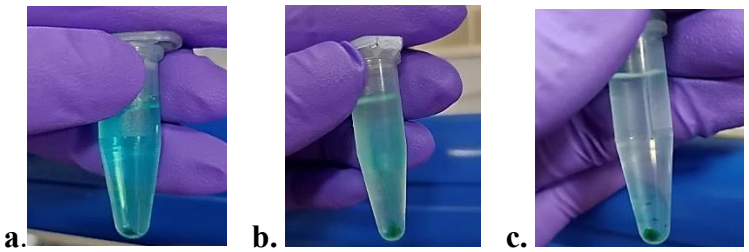

Figure 4.3. Different solvents have been used for the preparation of PLL NPs. (a) PLL NP in MQ, (b) PLL NP in DI, (c) PLL NP in PBS.

4.2.4 Optical characterization

Optical characterization techniques, such as spectroscopy, can identify the concentration and structure of any compound. This is essential for confirming the purity of a compound and for detecting the presence of specific elements. For determination of the concentration of ICG within the NPs we have used UV-visible spectroscopy and fluorescence microscopy. Further, to analyze the confirmational changes of PLL NPs in the presence of salt and ICG, we have used CD spectroscopy.

4.2.4.1 UV-visible spectroscopy

The electromagnetic spectrum comprises cosmic rays, gamma rays, X-rays, Ultraviolet rays (UV), Visible, infrared (IR), microwaves, radio waves, etc. UV-Vis spectroscopy utilizes only a small part of the electromagnetic spectrum. Different processes such as absorbance, fluorescence, transmission, scattering, etc. can occur on the interaction of electromagnetic radiation with matter.

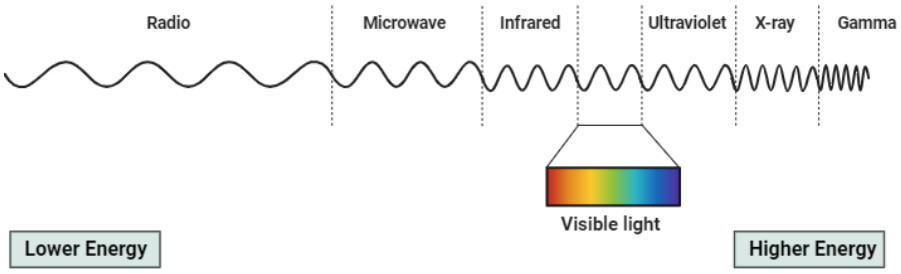

Figure 4.4. Electromagnetic spectrum [27]

UV-visible (UV-Vis) spectroscopy serves as a method for examining the absorption of ultraviolet and visible light by molecules. The fundamental principle of UV-visible spectroscopy revolves around the interaction of electromagnetic radiation with matter. The primary interaction between UV-Vis radiation and molecules occurs through electronic transitions. When the energy of incident light aligns

with the energy difference between two electronic states, molecules absorb energy and undergo electronic transitions. The energy levels of electrons within a molecule are quantized, and the absorption of UV-visible light induces electronic transitions from lower to higher energy states. The Beer-Lambert law, which links absorbance (A) to concentration (C), path length (l), and molar absorptivity (ε) of the absorbing species, determines how much light is absorbed by a sample. The equation is given by:

$$A=\varepsilon \cdot l \cdot C$$

Where:

- A represents the absorbance,
- ε represents the molar absorptivity (a constant for a given substance),
- l is for path length of the sample,
- C is the concentration of the absorbing species.

A UV-Vis spectrophotometer is the apparatus employed to measure the light absorbance of a sample. It comprises a light source, a monochromator for selecting a particular light wavelength, a sample holder, and a detector. The sample is positioned in the trajectory of the incident light, and the measured outcome involves the transmitted or reflected light. The instrument furnishes a spectrum depicting how absorbance changes in relation to wavelength.

By using UV-visible spectrophotometer, absorption spectra of free ICG and ICG with PLL NPs (supernatant & pellet with all the three solvents) were taken from 600nm to 1000nm with 1 nm slit width and 480 nm/s scan speed.

4.2.4.2 Fluorescence spectroscopy

Fluorescence spectroscopy relies on the fluorescence phenomenon, where energy transitions occur from a higher state to a lower state. For the emission of fluorescence,

molecules must be in a higher energy state to enable the emission process. This energy transition from a higher to a lower state can occur either through fluorescence (radiative) or phosphorescence (non-radiative). The emitted photons have a higher wavelength than the absorbed ones. Fluorescence spectroscopy involves essential components such as a light source (xenon lamp), two monochromators - one for adjusting the excitation wavelength and another for fluorescence emission—a sample holder, and detectors. Its primary purpose is to measure emission spectra by setting the excitation wavelength and scanning the wavelength throughout the emission spectra.

Fluorescence spectra of free ICG and encapsulated ICG (supernatant & pellet with all the three solvents) were taken at excitation wavelength 680nm and emission wavelength range from 700nm to 900nm by using Fluorimeter (Jobin Yvon Horiba, France) with excitation and an emission slit width of 1 nm.

4.2.4.3 Circular Dichroism Spectroscopy

Circular Dichroism (CD) spectroscopy is a technique that examines the absorption of circularly polarized light by molecules with asymmetry. In the far-UV range (180–250 nm), it proves valuable for evaluating the secondary structure of proteins by observing the rotation of phi and psi angles along the protein backbone. The protein's conformation influences these rotations, leading to distinct spectra that reveal structural elements.

CD spectra of PLL, PLL with salt aggregation & PLL with ICG in different solvents (Three different blanks used MQ, DI and PBS) were taken at the far-UV range (180-250 nm) with interval of 0.1 nm. All measurements were done in Quartz cuvette with 2 nm path length with slit width 1 nm and scanning time was 20 nm per minute.

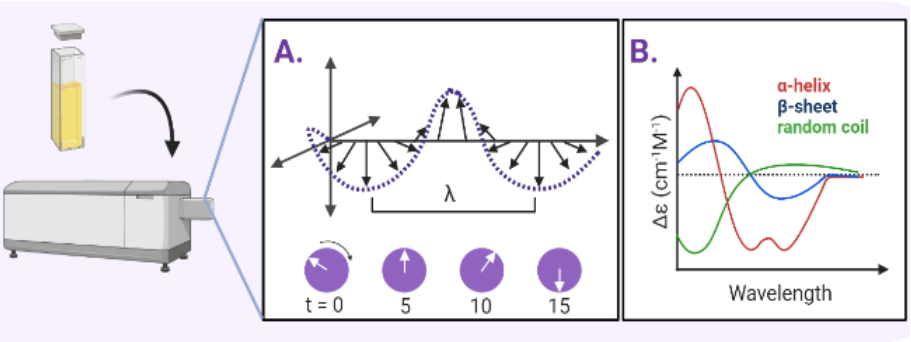

Figure 4.5. Predicting protein structure using circular dichroism spectroscopy

4.2.4.4 Morphological characterization

To examine the morphology of nanoparticles prepared in different solvents, PLL-ICG NPs were subjected to scanning electron microscopic analysis (Supra-55, Carl Zeiss, Sigma Series). Prior to electron microscopy, the suspension containing PLL-ICG NPs, was sonicated in a bath sonicator for 5 minutes and casted on a glass slide and left in a desiccator overnight to ensure proper drying of the sample. To enhance electron conductivity, the PLL NPs were sputter-coated with gold using a direct current (DC) sputter coater (Q-150RES, Quorem). SEM imaging was conducted at electron beam voltages 3-5 kV, capturing secondary electron images. Analysis of the field emission scanning electron microscopy (FESEM) images was performed using IMAGE J software (National Institutes of Health Bethesda, USA).

4.2.4.5 Estimation of encapsulation efficiency of nanoparticles

A direct method was used to test the nanoparticles' encapsulation efficiency. The first free ICG calibration curve in dimethyl sulfoxide (DMSO) was created. Following this, 1 mL of DMSO was added to each of the three pellets, and they were incubated for 60 to 90 minutes in order to release the ICG and disturb the nanoparticles. At a wavelength of 779 nm, the

absorption spectra of both nanoencapsulated and unbound ICG in DMSO were examined.

Encapsulation efficiency of the nanoparticles was calculated by the following formula-

EE% = (Concentration of ICG after disruption of NPs/ total concentration of ICG utilized during the NPs synthesis) *100

4.2.4.6 In-vitro drug release study

The pellets from each of the three samples were moved to the dialysis membrane and suspended in PBS, DI water, and MQ water (5 mL release medium) at a temperature of 25°C. After that, the dialysis membrane was added to a 100 mL glass cylinder filled with release media, and the mixture was shaken with a magnetic stir bar at 200 rpm. The amount of drug released was measured by taking sporadic (1 mL) samples from the outer media. The media was changed out right away following the sample. A UV-visible spectrophotometer was used to measure absorbance at various times to determine the amount of dye released.

4.2.4.7 Measurement of temperature elevation in bare nanoparticles

To demonstrate the photothermal activity, a series of experiments were conducted using various samples in 96-well plates. These samples included MQ water, DI water, and PBS, serving as control solutions. Additionally, three different types of PLL-ICG NPs, each at varying dilutions (5, 10, 15, 20, 25 and 30 % V/V), were prepared and included in the experimental setup. Each sample in the 96-well plates was irradiated with a near-infrared (NIR) laser (808 nm) and a power density of 7.746 W cm−2. The irradiation was performed for different time points (1, 2, 3, 4 and 5 minutes), allowing for the assessment of temperature changes induced by the photothermal effect. Temperature measurements were taken using a thermometer, providing quantitative data on the thermal response of each

sample to NIR laser irradiation. Additionally, infrared thermal imaging was done of all the samples after laser irradiation. This comprehensive experimental setup enabled the evaluation of the photothermal activity of the samples, shedding light on the efficacy of PLL-ICG NPs as potential agents for photothermal therapy.

4.2.4.8 Cell culture

MCF-7 cell line was used for all in-vitro cellular studies. DMEM media with 1% Penicillin-streptomycin, 1% L-glutamine and 10% foetal bovine serum (FBS) was used to grow cells. MCF-7 cells were cultured and incubated in a humidified environment with 5% carbon dioxide (CO2) at 37°C. The cells were detached with 0.25% trypsin-EDTA and subcultured when they achieved around 80% confluency.

4.2.4.9 Cell viability assay and cellular uptake of PLL-ICG NPs

10,000 live MCF-7 cells per well were seeded in 96-well plates and allowed to grow for 24 hours. After 24 hours, samples were treated with newly prepared PLL-ICG NP at various concentrations (5, 10, 15, 20, 25 and 30μM) of ICG and incubated at 37°C for another 24 hours. The cells with only DMEM media and no nanoparticles was used as a positive control. The PLL-ICG NPs' viability was assessed using the standard MTT assay. Following a 24-hour incubation period, 200 μL of MTT solution (0.5 mg/mL) was added in each well after aspirating off the nanoparticle suspension. After four hours of incubation, 100 μL of dimethyl sulfoxide (DMSO) was given to each well to dissolve the insoluble formazan crystals that the living cells had formed. The absorbance measurements were made at 570 nm using the UV-Vis microplate spectrophotometer (SynergyH1, BioTek). The percentage drop in viability with respect to untreated (control) cells was used to compute the cellular viability.

NIR fluorescence imaging was carried out to evaluate the uptake of PLL-ICG NPs by the MCF-7 cells. MCF-7 cells were cultured and seeded in a 12 well plate (70000 cells/well) and were allowed to adhere for 24h. After 24h, the media was aspirated off and cells were washed 3-4 times with 1X PBS to remove unbound particles. Following this, cells were then incubated with different concentrations of PLL-ICG NPs prepared in PBS, DI, MQ and free ICG along with plain media control (untreated cells) for 6 h in an incubator at 37 °C with 5% CO2 supply. Following incubation, the cell culture media was removed, and cells were washed thrice with 1x PBS. Cell fixation was done using 4% paraformaldehyde (PFA) for 20 minutes at room temperature. After 20 minutes, PFA was removed and again the cells were washed thrice using 1X PBS. The nucleus of the cells was then stained using 1µg/mL of DAPI. The cells were washed again with 1X PBS to remove extra dye. The NIR fluorescence imaging of MCF-7 cells was performed using Nikon Eclipse Ti-U inverted microscope. The cells were then visualised using Nikon Eclipse Ti fluorescence microscope equipped with xenon & mercury lamps along with Ultraviolet & NIR filter cubes. The ICG shows emission in near-infrared window while DAPI shows blue emission in visible range.

4.2.4.10 Assessment of cell viability after laser treatment

MCF-7 cells were seeded in 96-well plates (10,000 cells/ well) and grown in complete DMEM media for 24 h. Following the incubation, the media was then replaced with fresh media containing different concentrations of PLL-ICG NPs. 6 h of incubation period was given, following which, cells were irradiated with 808 nm laser (7.746 Watt cm-2) for 5 min and the cell viability was determined by MTT assay.

4.2.4.11 ROS generation assay

For the detection of ROS (reactive oxygen species) generation in MCF-7 cells after laser treatment, DCFDA (2',7'-dichlorodihydrofluorescein diacetate) was used. DCFDA is a cell-permeable, non-fluorescent compound that diffuses into cells. Once inside the cell, it is hydrolyzed by intracellular esterases to form DCFH (2',7'-dichlorodihydrofluorescein), which is unable to diffuse out of the cell. Once DCFH is formed, it reacts with ROS present in the cells, primarily hydrogen peroxide (H2O2), hydroxyl radicals (·OH), and peroxynitrite (ONOO-), to form the fluorescent product DCF (2',7'-dichlorofluorescein). DCF is highly fluorescent and emits green fluorescence when excited by light at a specific wavelength. Thus, the intensity of the fluorescence emitted is directly proportional to the amount of ROS generated within the cell.

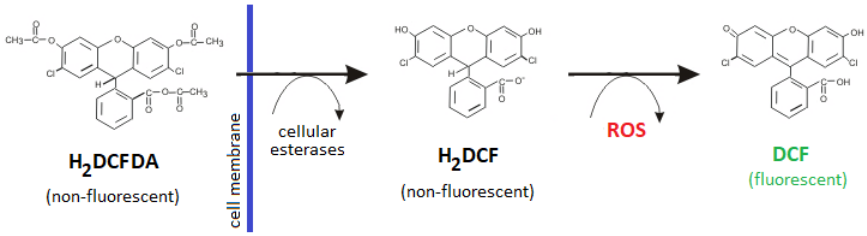

Figure 4.6. Mechanism of DCFDA in ROS generation assay.

For this experiment, 15000 cells were seeded and incubated with 15 µM of PLL-ICG NPs for 6 hours followed by laser irradiation. Control cells are irradiated with laser and stained with DCFDA dye.

4.2.4.12 Calcein and Propidium Iodide (PI) Staining (Live-dead assay)

Calcein-AM and propidium iodide (PI) co-staining was done to assess the ratio of live and dead cells post incubation with PLL-ICG NPs and laser treatment. Calcein-AM is a non-fluorescent, cell-permeant compound that freely enters cells. Once inside the cell, esterases cleave the AM (acetoxymethyl) groups from Calcein-AM, resulting in the formation of Calcein, which is a

green fluorescent molecule. Calcein is well retained within live cells due to its hydrophilic nature. PI is a red fluorescent dye that is impermeable to live cells but can penetrate cells with compromised cell membranes, such as dead or dying cells. PI intercalates with nucleic acids (DNA and RNA) and emits red fluorescence upon binding. Live cells with intact membranes hydrolyze Calcein-AM to form green-fluorescent Calcein, and they appear green under fluorescence microscopy. Dead or dying cells with compromised membranes allow PI to enter and bind to nucleic acids, resulting in red fluorescence.

For this experiment, 15000 cells per well were seeded and incubated with 15 μM of PLL-ICG NPs for 6 hours. Cells without any treatment was taken as a control. After that, cells were irradiated with laser and co-stained with Calcein and PI.

Chapter-5
Results and Discussion

Analysis of UV-visible spectroscopy data offers a comprehensive understanding of the optical properties and presence of ICG within the nanoparticles. In the spectral analysis of these nanoparticles, distinct variations in absorption peak intensity were observed among the different solvents utilized.

5.1 Spectroscopic analysis

The absorption spectra of free ICG and PLL-ICG NPs prepared in different solvents were measured from 500 nm to 1000 nm. In figure 5.1, the absorption spectra of free ICG dispersed in MQ water and PLL-ICG NPs prepared in MQ water, DI water and PBS are shown. Figure 5.1 a shows the absorption spectra of free ICG, which has an absorption maximum at 780 nm with a shoulder at 695 nm, which corresponds to the absorbance of the aggregated and monomer form of ICG molecule, respectively. For NPs prepared in MQ water, we observed poor encapsulation efficiency of ICG, as shown in the figure 5.1 b the absorbance of supernatant is much higher than the pellet. In contrast, pellet of DI water showed moderate absorption peak intensity with blue shift (H-aggregation) and red shift (J-aggregation), reflecting a somewhat improved spectral response relative to MQ water (Figure 5.1 c). This suggests that DI water may offer conditions more conducive to nanoparticle formation. NPs prepared in PBS demonstrated the highest intensity of absorption peaks, three absorption maxima are present at 695 nm, 779 nm and 850 nm, which corresponds to the absorbance of H-aggregated, monomeric and J-aggregated form of ICG (Figure 5.1 d). The pronounced spectral response observed in PBS indicates favourable conditions for efficient nanoparticle formation and encapsulation efficiency of ICG.

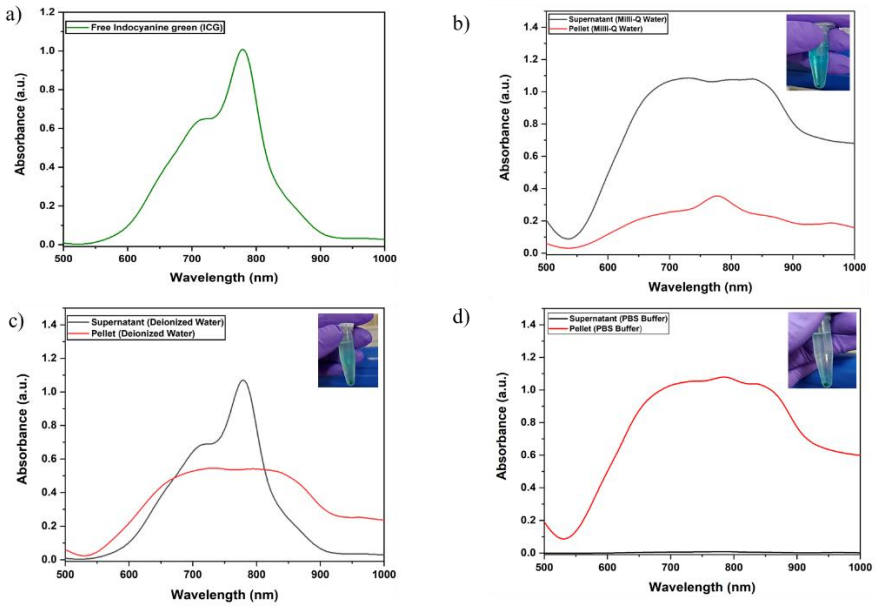

Figure 5.1. Absorption spectra of ICG & PLL-ICG nanoparticles (a) Free ICG. (b) PLL-ICG nanoparticles in MQ water. (c) PLL-ICG nanoparticles in DI water. (d) PLL-ICG nanoparticles in PBS.

In the assessment of fluorescence emission spectra corresponding to nanoparticle synthesis in various solvents, distinct trends in emission intensity were observed. The emission spectra were recorded in the range of 750 nm to 850 nm following the excitation of samples at 680 nm. Figure 5.2 a shows the emission spectra of free ICG, which has maximum emission peak intensity at 805 nm. Pellet prepared in MQ water showed the least intensity of fluorescence emission, indicative of the least spectral response compared to the other solvents (Figure 5.2 b). This outcome suggests that the conditions provided by MQ water are not favourable for these NPs. Conversely, pellet formed in DI water exhibited a moderate fluorescence emission intensity, suggesting a somewhat improved spectral response relative to MQ water (Figure 5.2 c). This implies that DI water may offer conditions more conducive to pellet formation, although to a lesser extent than PBS. Notably, pellet prepared in PBS demonstrated the highest intensity of fluorescence emission (Figure 5.2 d). The pronounced spectral response observed in PBS indicates favourable conditions for efficient fluorescence emission from the synthesized nanoparticles due to maximum amount

of encapsulated ICG. Overall, these findings underscore the significant influence of solvent selection on fluorescence emission characteristics during nanoparticle synthesis.

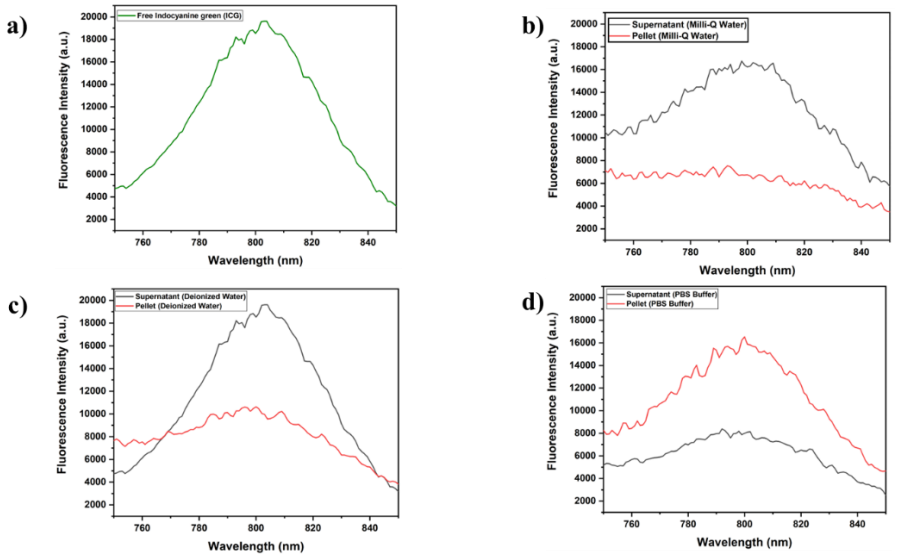

Figure 5.2. Emission spectra of ICG & PLL-ICG nanoparticles (A) Free ICG (B) PLL-ICG nanoparticles in MQ water (C) PLL-ICG nanoparticles in DI water (D) PLL-ICG nanoparticles in PBS.

To understand the interaction of ICG with PLL and salts we have used circular dichroism (CD) spectroscopy was used to look at how ICG and salt affected PLL NP assembly. Figure 5.3 shows CD spectra of PLL in water, PLL in a salt solution, and PLL NPs. PLL alone show's random coil conformation is shown in its CD spectrum, which have a single negative band at about 207 nm and a positive band at about 218 nm. The band intensity increases at 207 nm and decreases at 218 nm with the addition of the salt solution, indicating a possible interaction between PLL molecules and salts. When ICG is added to the PLL-salt complex, the peak at about 207 nm becomes more intense, whereas the peak at about 218 nm becomes less intense. The growth formation of more complex structure in the form of nanostructure is confirmed by these shifts in the CD spectrum of PLL-ICG NPs, which indicate an active interaction between ICG and PLL molecules that results in the construction of a stable nanostructure. Furthermore, small changes in the band within the PLL structure were noted in several different

solvents, suggesting that the structure of PLL strands is affected by a variety of solvents (with different ion concentrations). This difference might be due to the difference in the ionic strength of these solvents.

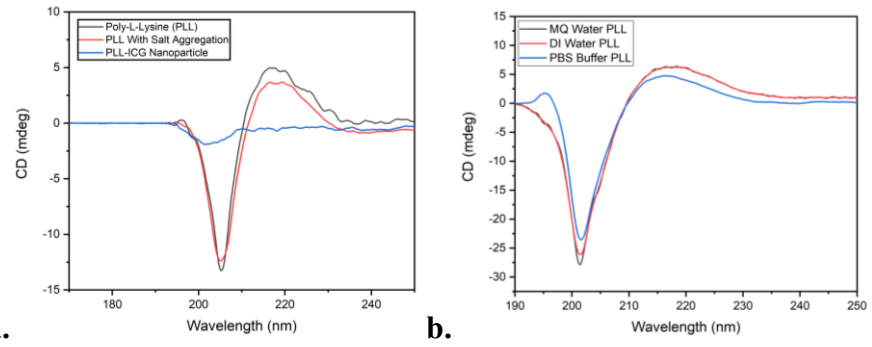

Figure 5.3. (A) CD spectra of PLL and its interaction with salt and ICG. (B) CD spectra of PLL and its interaction with different solvents.

5.2 Morphological characterization

Morphological assessment of nanoparticles in different solvents was done by scanning electron microscopy (SEM), which revealed notable disparities among the nanoparticle samples produced in different solvents. The nanoparticles synthesized in MQ water exhibited a size distribution with an average diameter of approximately 150 nm. However, despite this relatively smaller size, they demonstrated comparatively lower stability and lesser formation compared to those produced in solvents DI water and PBS. This observation suggests that MQ water may not be optimally conducive to the nucleation and growth of nanoparticles or may introduce unfavourable conditions leading to aggregation or inadequate stabilization of nanoparticles. In contrast, nanoparticles synthesized in DI water exhibited a larger size distribution with an average diameter of approximately 235 nm. Despite this larger size, they demonstrated moderate results in terms of stability and formation, indicating an intermediate level of performance relative to solvents MQ water and PBS. Conversely, NPs synthesized in PBS demonstrated a size distribution with an average diameter of approximately 165 nm. These nanoparticles exhibited superior stability and maximal formation, indicating that PBS may offer favourable

conditions for the nucleation and growth of nanoparticles, thereby promoting their stability and enhancing their yield. The observed variations in stability and formation among the nanoparticle samples synthesized in different solvents underscore the critical influence of solvent selection on nanoparticle synthesis processes. Understanding and optimizing these solvent-dependent parameters are pivotal for the rational design and fabrication of nanoparticles with desired properties for diverse applications.

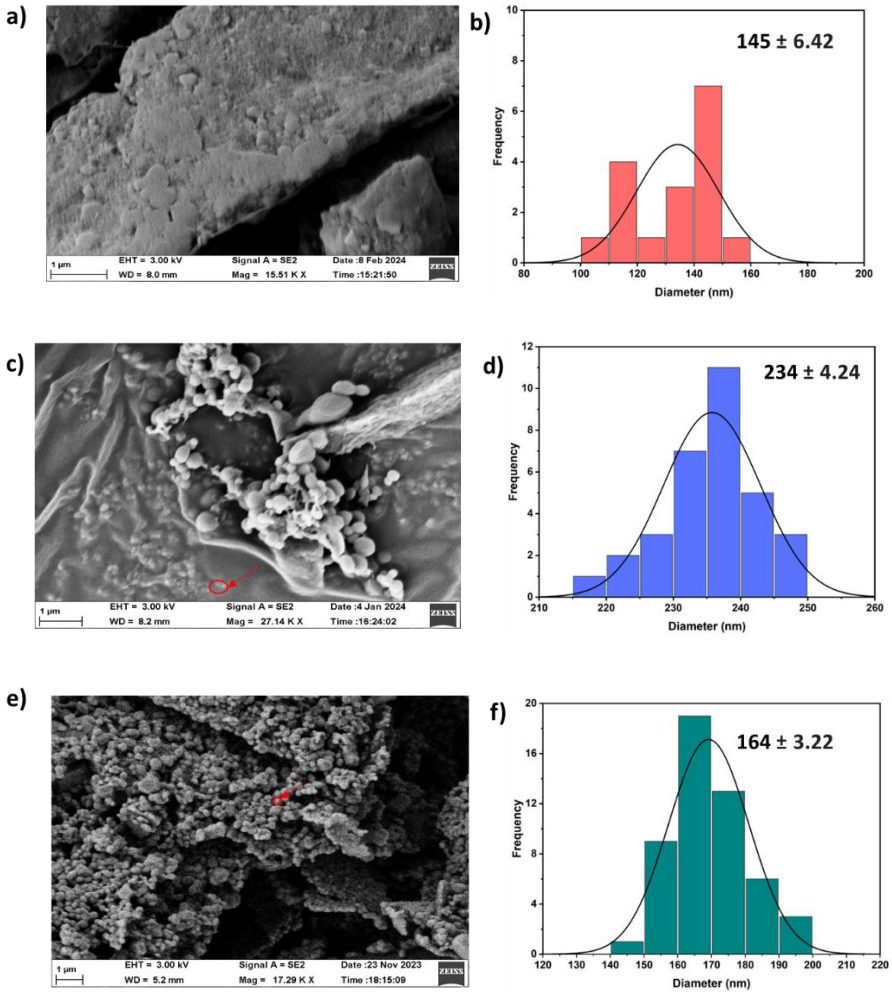

Figure 5.4. SEM analysis of PLL-ICG nanoparticles' morphology. (a-b) SEM image of PLL NPs in MQ. (c-d) SEM image of PLL-ICG NPs in DI. (e-f) SEM image of PLL-ICG NPs in PBS.

5.3 Encapsulation efficiency

For the calculation of encapsulation efficiency of NPs in different solvents, λ max of ICG-DMSO absorption spectrum was observed

around 779 nm (because free monomeric ICG gives maximum absorption spectra at this wavelength). So, the absorbance of ICG encapsulated PLL NP on the addition of DMSO was recorded at 779 nm and found that in case of MQ water the concentration was 9.47 µM and encapsulation efficiency was found to be 7.34%, while in DI water the concentration was 28.67 µM and encapsulation efficiency was 22.22%, on the other hand, PBS shows the maximum encapsulation efficiency which is 42.63% and concentration was found to be 55.43 µM.

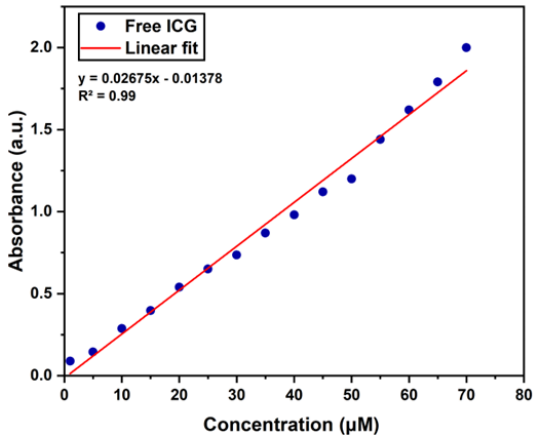

Figure 5.5. Calibration curve of free indocyanine green (ICG) in dimethyl sulfoxide (DMSO).

Sample	Concentration (micromolar)	Mean (n = 3)	EE%	EE% ± SD
PBS buffer	53.5	55.43	42.63	**42.63 ± 2.6**
	52.21			
	60.58			
DI water	29.74	28.67	22.22	**22.22 ± 0.63**
	28.55			
	27.73			
MQ water	9.31	9.47	7.34	**7.34 ± 0.23**
	9.93			
	9.18			

Table 5.1. Concentration and EE% of all the PLL-ICG NPs in their respective solvents.

5.4 In-vitro release study

To check the stability of the PLL-ICG NPs in their respective solvent, we have performed the in-vitro release study. In this experiment, MQ

water showed the maximum % cumulative release of the ICG as it contains a very small amount of PLL NPs, while in the case of PBS buffer and DI water, it showed a very small release. Here in table 5.2, we can see that cumulative % cumulative release of ICG is very high in case of MQ followed by DI and PBS. In conclusion, NPs prepared in PBS buffer show very little leaching, while NPs in MQ water show maximum leaching effect with respect to time.

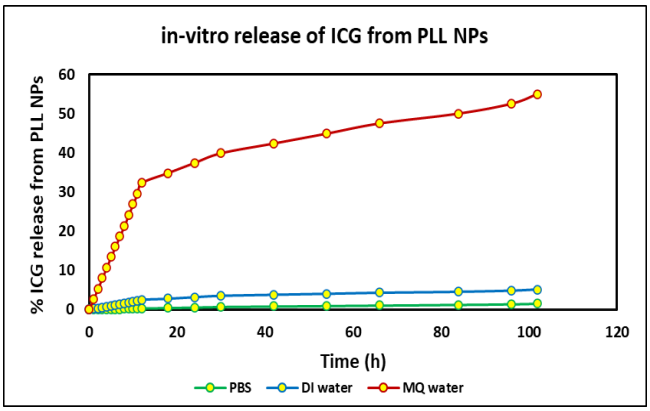

Figure 5.6. Cumulative percentage ICG release from PLL NPs in different solvents. MQ showed the maximum release of ICG from NP with respect to time followed by DI and PBS.

Time (hr)	PBS buffer	Deionized water	Mill-Q water
6	0.1226	1.1501	16.049
12	0.3201	2.5364	32.32
24	0.5544	3.1878	37.45
42	0.8147	3.795	42.396
84	1.231	4.549	50.022
102	1.5095	5.145	55.028

Table 5.2. Cumulative % release of ICG at different time points.

5.5 Photothermal efficiency of bare nanoparticles

The efficacy of photothermal therapy (PTT) relies significantly on its ability to efficiently generate heat. To assess the photothermal

properties of PLL-ICG NPs in different solvents under 808 nm irradiation, their performance was examined across various dilutions (% V/V). PTT efficiency of all three bare nanoparticles was measured at a constant power density of 7.746 W cm−2. The initial temperature was 24 °C. In this experiment, we found that NPs prepared in MQ water showed the least temperature difference (ΔT_{max} = 8 °C), in DI water it was 12 °C (Figure 5.7 b).

It was observed that the photothermal effectiveness of PLL-ICG NPs prepared in PBS was very high upon the intensity of the irradiation as it shows the highest encapsulation efficiency. Specifically, upon 5 minutes of irradiation at a power density of 7.746 W cm−2, the temperature of the PLL-ICG NPs in the PBS increased by 18 °C (Figure 5.7 c). Further, PTT efficiency of PLL-ICG NPs prepared in PBS was measured at different concentrations (5, 10, 15, 20, 25 and 30 μM) for different time points (1, 2, 3, 4 and 5 minute) and observed the maximum temperature change which is 22 °C. With this result, we can conclude that PBS is the most suitable solvent for the preparation of PLL-ICG NPs, as it showed the maximum encapsulation efficiency and temperature elevation.

After that IR thermal imaging was done of the NPs post laser irradiation, which showed that with the increasing concentration of ICG , temperature difference is also increasing. Here PBS showed the maximum temperature rise followed by DI and MQ (Figure 5.8).

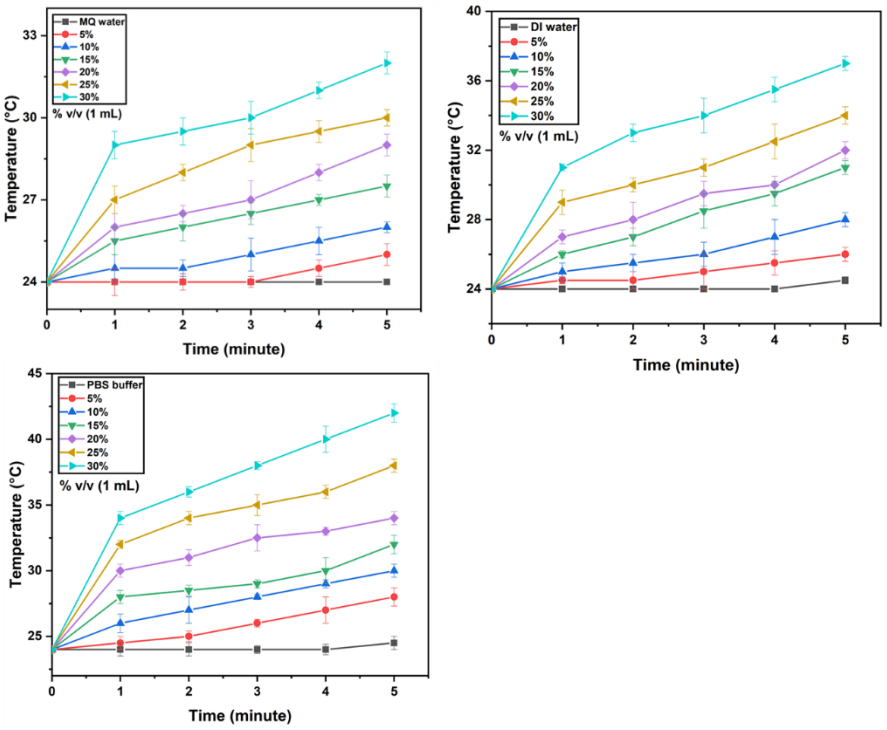

Figure 5.7. Photothermal efficiency curve of PLL-ICG NPs at different time points (for 1, 2, 3, 4, and 5 minutes) of laser irradiation (808 nm, 0.55 W). All experiments were conducted at different dilutions (5, 10, 15, 20, 25, and 30% V/V, total volume is 1 mL) based on the ICG content. (a) PTT efficiency of PLL-ICG NPs in MQ water. (b) PTT efficiency of PLL-ICG NPS in DI water. (c) PTT efficiency of PLL-ICG NPs in PBS.

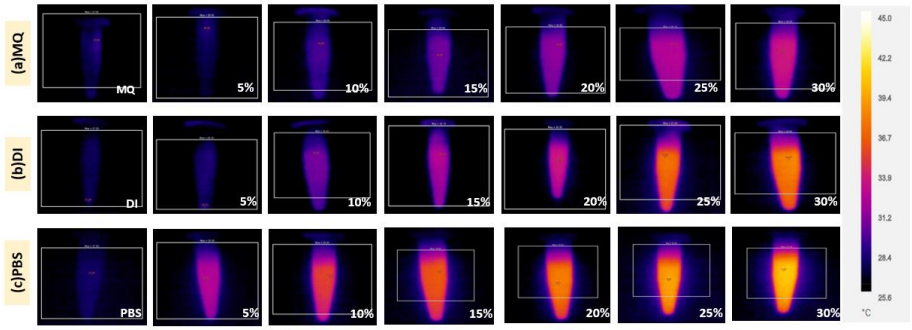

Figure 5.8. Infrared thermal images of PLL-ICG nanoparticles made using (a) MQ, (b) DI, and (c) PBS, post irradiation with 808nm laser at 0.55 watt for 5 minutes each. Power density was 7.746 watt/cm^2. %V/V dilutions were made after resuspending the pellets obtained in each

case in 1 mL of respective solvents (MQ, DI, and PBS). The increase in concentration of ICG causes the temperature to rise synonymously.

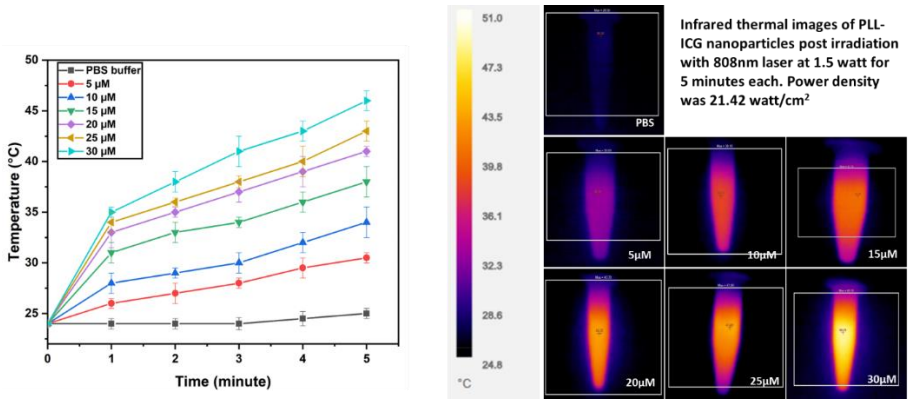

Figure 5.9. Photothermal efficiency curve of PLL-ICG NPs prepared in PBS (a) PTT efficiency at different concentrations (5, 10, 15, 20, 25, and 30 µM) (b) IR thermal image of NPs after laser irradiation.

5.6 Cytotoxicity assay

It is necessary to determine these NPs' safety for their biological applications. The MTT assay was used to assess in vitro cytotoxicity of PLL-ICG NPs. The outcome of the cell viability experiment, in which MCF-7 cells were cultured for 24 hours with varying concentrations of PLL NPs, free ICG, and PLL-ICG NPs (in PBS buffer, which demonstrates the maximum encapsulation efficiency), is displayed in Figure 8a. PLL NPs have an estimated IC_{50} of 11.85 µg/mL, whereas free ICG has an IC_{50} of 39.34 µM (Figure 5.10 b). The viability of the cells treated with PLL-ICG NPs at concentrations of 15 µM and 20 µM is approximately 80% and 75%, respectively. When cells were incubated with 25 µM and 30 µM of PLL NPs, cellular viability decreased; these cells displayed ~60% and less cellular viability, with an estimated IC_{50} of 36.82 µg/mL (Figure 5.10 c). As a positive control, MCF-7 cells that had not received any treatment were employed. This suggests that PLL-ICG NPs can be safely used as a delivery mechanism, as mentioned for biological purposes. Following the cell viability experiments were carried out to explore the potential of PLL-ICG NPs for pharmaceutical or contrast agent delivery applications.

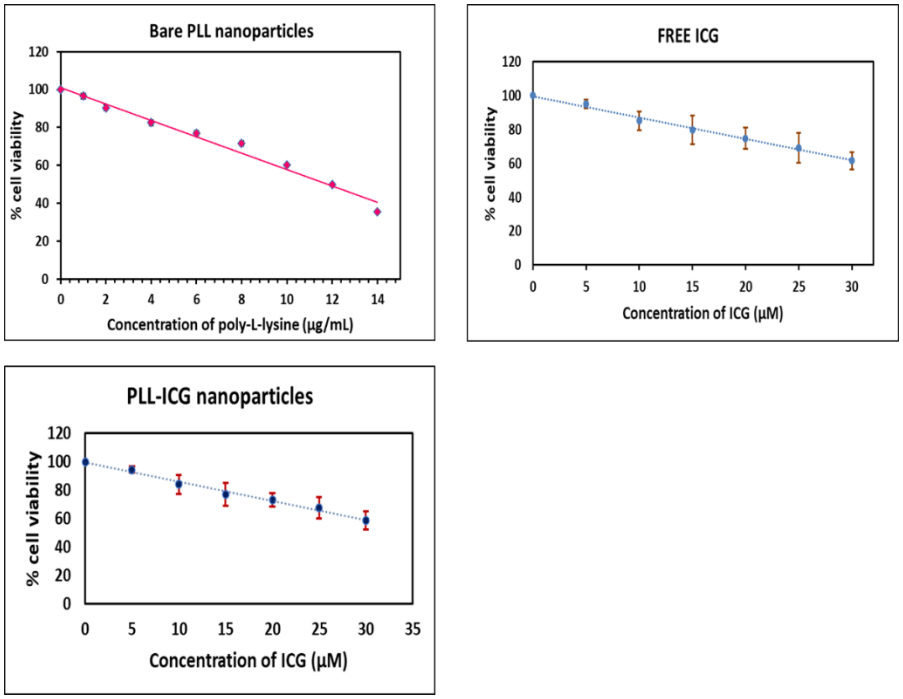

Figure 5.10. in-vitro cytotoxicity analysis of (a) Bare PLL nanoparticles performed in biological duplicate (b) Free ICG performed in biological quadruplicate, and, (c) PLL-ICG nanoparticles (in PBS) performed in biological quintuplicate; on MCF-7 cells for 24h at a seeding density of 1×10^4 cells per well.

5.7 Cellular uptake study

The cellular uptake capacity of nanoparticles (NPs) plays a crucial role in photothermal therapy (PTT) efficacy. In this study, MCF-7 cells were exposed to varying concentrations (10 µM and 15 µM) of PLL-ICG NPs for 6 hours. Following incubation, the cells were stained with DAPI (resulting in blue colour) and visualized using fluorescence microscopy. The fluorescence imaging revealed the presence of near-infrared (NIR) fluorescence emitted by PLL-ICG NPs within the cells, indicating successful internalization by the cells. Notably, cells treated with PLL-ICG NPs exhibited stronger fluorescence compared to those treated with free ICG. Conversely, no fluorescence was detected in the control group cells. On the other hand, NPs prepared in PBS showed higher fluorescence followed by DI and MQ as PBS contains higher concentration of ICG. The robust

uptake of PLL-ICG NPs suggests efficient encapsulation facilitated by PBS, and the enhanced fluorescence underscores the superiority of PLL-ICG NPs over free ICG for fluorescence imaging. Moreover, the fluorescence intensity of PLL-ICG NPs exhibited a direct correlation with the concentration of ICG. This observation was further confirmed through quantitative fluorescence analysis of fluorescence images, reinforcing the notion of PLL-ICG NPs possessing exceptional cellular uptake capabilities. Overall, these findings emphasize the remarkable cellular uptake ability of PLL-ICG NPs, highlighting their potential for advanced biomedical applications. Also, we have compared the cellular uptake of all three NPs in their respective solvent. NPs prepared in PBS showed maximum cellular uptake followed by DI and MQ.

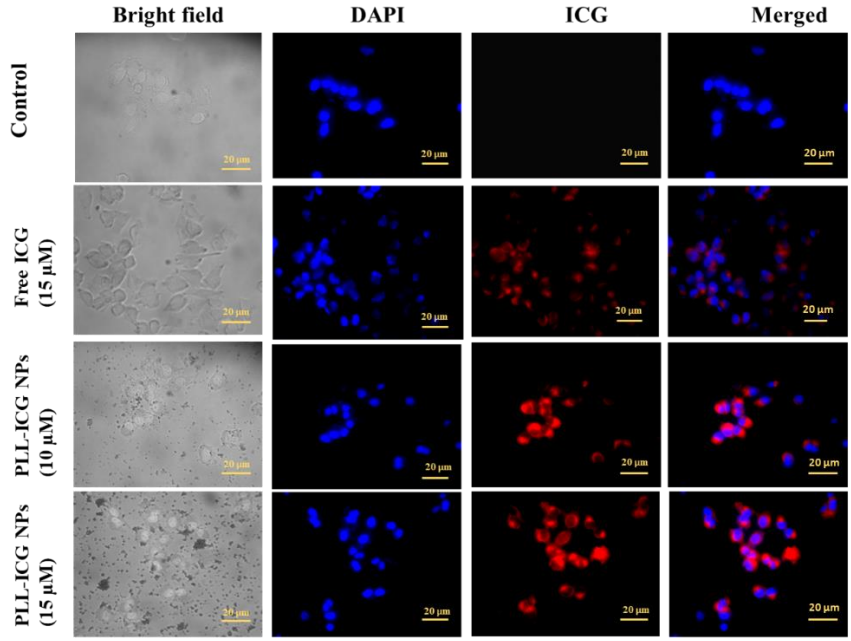

Figure 5.11. In-vitro cellular uptake. MCF-7 cells incubated with two different concentrations of PLL-ICG NPs (with ICG concentrations in it as 10 µM and 15 µM respectively) and free ICG (15 µM) for 6 h, fixed with 4% PFA, and nucleus stained with DAPI. The fixed cells were then excited by mercury and xenon lamps for ICG and DAPI excitation, respectively, using Nikon Eclipse Ti-U inverted microscope system. The red color denotes ICG uptake in cytoplasm while blue color shows DAPI stained live nucleus.

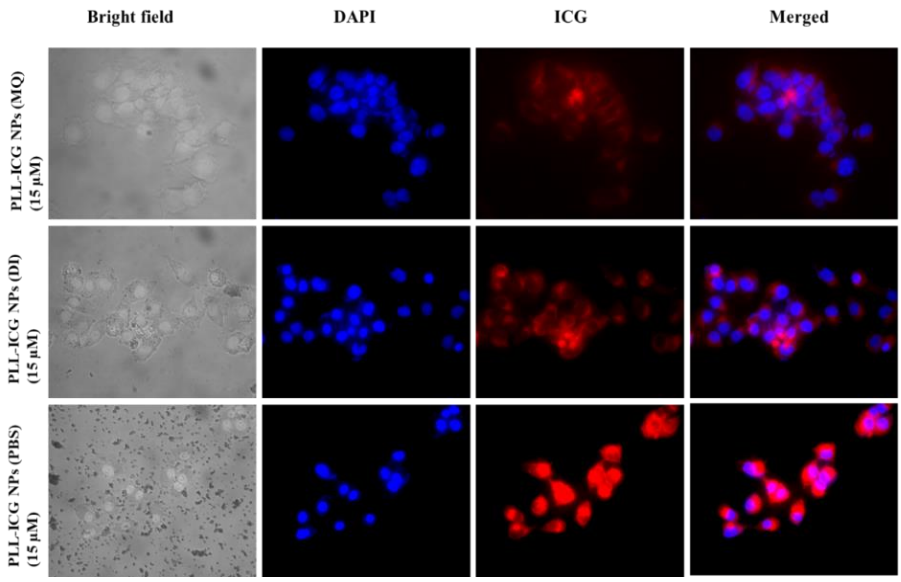

Figure 5.12. Comparative assessment of cellular uptake of PLL-ICG NPs made in MQ water, DI water and PBS. MCF-7 cells were incubated with 15 µM of PLL-ICG NPs prepared in MQ, DI and PBS for 6 h and stained with DAPI. The red color denotes ICG uptake in cytoplasm while blue color shows DAPI stained live nucleus.

5.8 MTT assay after In-vitro photothermal therapy

The evaluation of photothermal-induced cytotoxicity by PLL-ICG NPs was conducted following irradiation with an 808 nm laser at a power density of 7.746 W cm-2 for a duration of 5 minutes. Notably, the treatment with the laser alone did not induce any significant cytotoxicity, suggesting that the laser irradiation itself did not adversely affect cell viability. However, when MCF-7 cells were exposed to PLL-ICG NPs under the specified irradiation conditions, a considerable level of cell death exceeding 50% was observed. These findings underscore the potent cytotoxic effect exerted by PLL-ICG NPs in response to laser irradiation, highlighting their ability to induce cell death through efficient photothermal heating. Importantly, these results affirm the safety of PLL-ICG NPs in the absence laser treatment while emphasizing their potential as effective agents for photothermal therapy (PTT), wherein laser-triggered cytotoxicity can be precisely controlled and targeted, offering promising prospects for the treatment of cancer and other diseases.

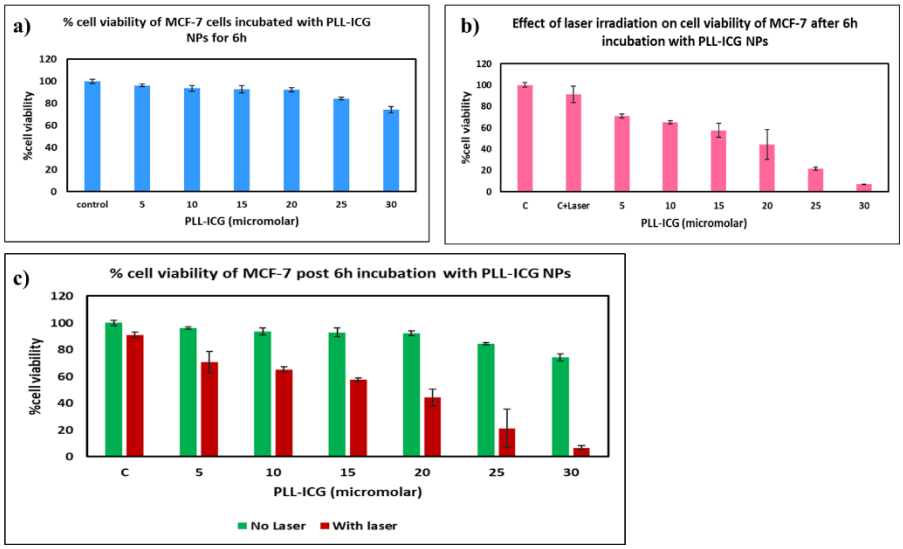

Figure 5.13. In-vitro photothermal cytotoxicity. MTT assay of MCF-7 post laser irradiation (a)% cell viability of MCF-7 cells (seeding density= 1×10^4 cells/well) post 6h incubation with different concentrations of PLL-ICG NPs. (b)% cell viability of MCF-7 cells (seeding density= 1×10^4 cells/well) post 6h incubation with different concentrations of PLL-ICG NPs followed by laser irradiation (0.55 watt for 5 minutes each). (c) Comparative assessment of % cell viability of MCF-7 cells before and after laser irradiation.

5.9 Live-dead assay

For the live-dead cell imaging, the cells were co-stained with Calcein and PI. Calcein binds with live cells and gives green fluorescence, while PI binds with the nucleus of dead cells and gives red fluorescence. Here, in the first row, we have taken untreated cells as a control. The consecutive rows show cells treated with PLL-ICG NPs for 6h, with and without laser irradiation. In conclusion, we can say that the synthesized nanoparticles shows less cellular toxicity and exhibits apoptotic potential only after being exposed to laser irradiation.

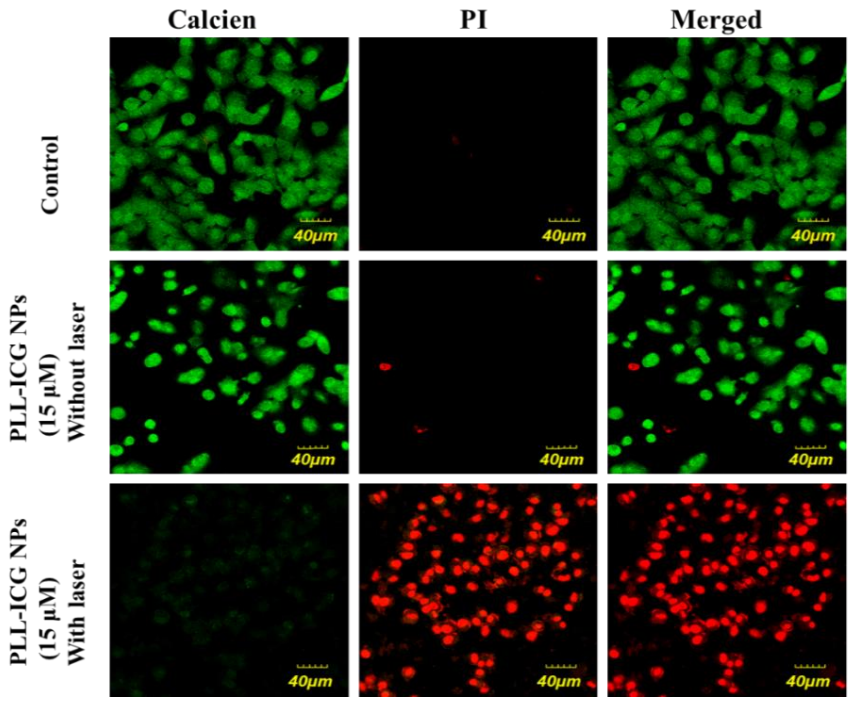

Figure 5.14. MCF-7 cells, costained with Calcein and PI. (a) Control cells, (b) Cells treated with PLL-ICG NPs without laser irradiation, (c) Cells treated with PLL-ICG NPs and laser.

We also analyzed the PTT potential of synthesized PLL-ICG NPs on the 3D-cell models of MCF-7. Untreated control is irradiated with laser and costained with Calcein and PI and we observed that most of the cells are still viable. On the other hand, these 3D-cell models were incubated with PLL-ICG NPs followed by laser irradiation and we observed a significant decrease in live cells.

5.10 ROS generation assay

For ROS generation study we have used DCFDA stain. Figure 5.17 a shows control cells with laser treatment and as expected there is no fluorescence observed. But in case cells treated with PLL-ICG NPs followed by laser irradiation the cell shows green fluorescence (Figure 5.17 b), this is due to PDT efficiency of ICG. When ICG is treated with laser transfers its energy to molecular oxygen and converts it into singlet oxygen (ROS). In the presence of ROS DCF gives green fluorescence.

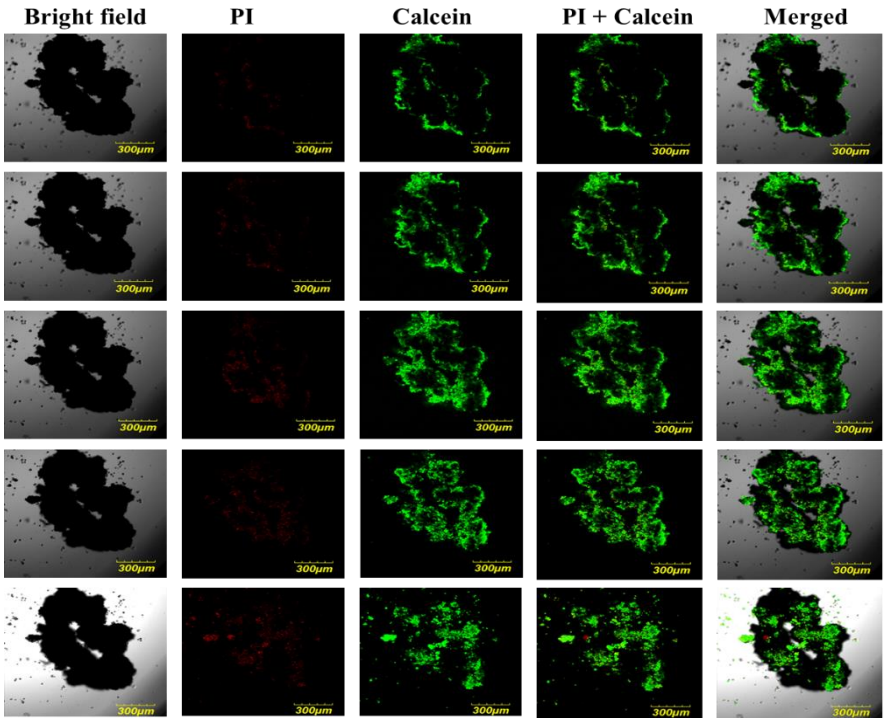

Figure 5.15. Confocal Z-stack fluorescence images of 3D-cell model of MCF-7 cells irradiated with 808 nm laser and co-stained with Calcein and PI.

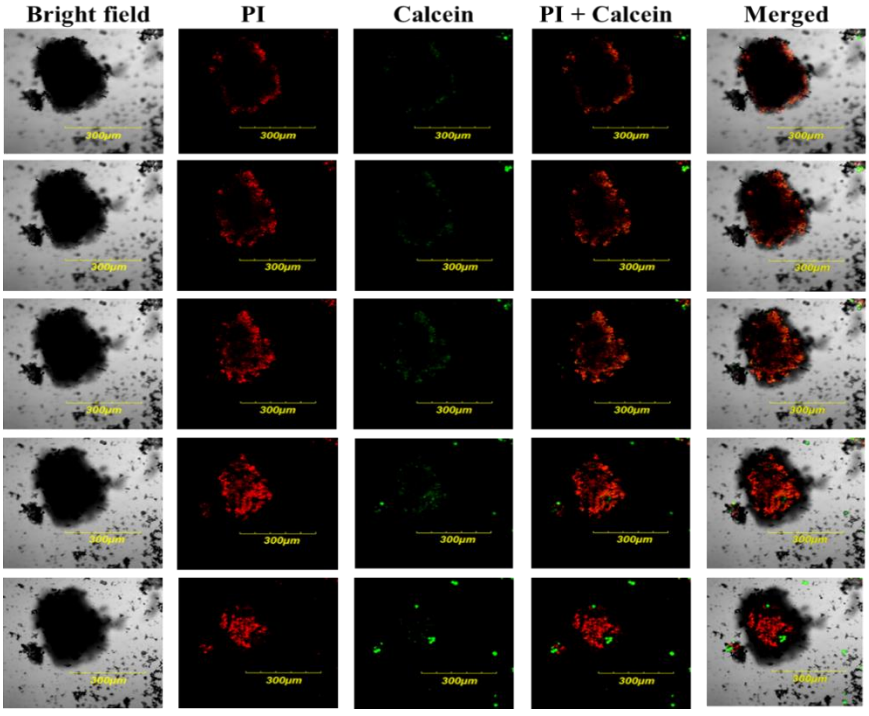

Figure 5.16. Confocal Z-stack fluorescence images of 3D-cell model of MCF-7 cells post 6h incubation with PLL-ICG NPs followed by

laser irradiation using 808 nm NIR laser. The cells were then co-stained with Calcein and PI.

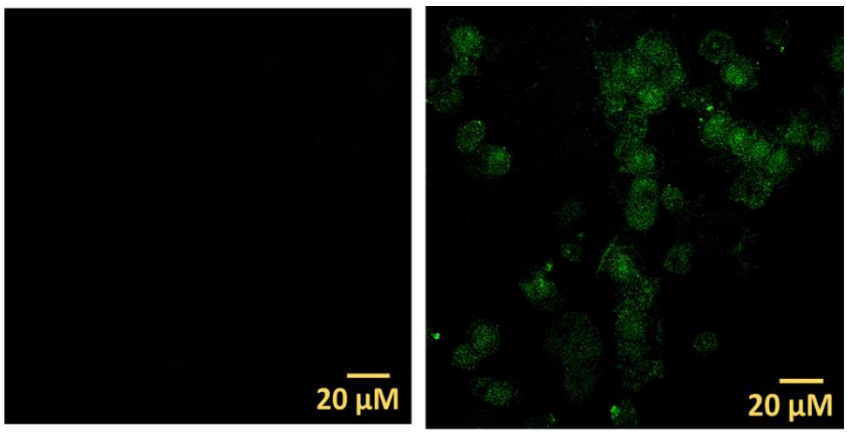

Figure 5.17. MCF-7 cells stained with DCFDA dye to record laser induced ROS generation in presence of ICG. (a) Control cells (live) with only DMEM media irradiated with 808 nm laser shows no ROS generation, (b) Cells treated with PLL-ICG NPs followed by laser irradiation gives green fluorescence due to ROS generation.

Chapter – 6
Conclusion and future scope

6.1 Conclusion

In conclusion, the synthesis and characterization of Poly-L-lysine (PLL) based nanoparticles containing Indocyanine Green (ICG) hold significant promise for biomedical applications, particularly in the field of photothermal therapy (PTT). Through a systematic investigation, we have elucidated the role of solvent selection in modulating the different properties and therapeutic efficacy of these nanoparticles, shedding light on critical factors influencing their performance for cancer therapy. Our findings demonstrate that the choice of solvent during nanoparticle synthesis profoundly impacts key parameters such as morphology, size distribution, stability, and loading efficiency. By carefully selecting the solvent system, we can tailor the properties of PLL-ICG nanoparticles to optimize their therapeutic outcomes, including efficient cellular uptake, and potent photothermal ablation of cancer cells. Cell culture experiments have provided valuable insights into the biocompatibility, cytotoxicity, and cellular uptake kinetics of PLL-ICG nanoparticles, laying the groundwork for their further development as effective nanotherapeutic agents. The demonstrated cytocompatibility and cellular uptake efficiency underscore the potential of these nanoparticles for targeted drug delivery and imaging applications, in addition to PTT. Furthermore, our study highlights the versatility of PLL-based nanoparticles as a platform for integrating multifunctional components and achieving synergistic therapeutic effects. Future directions may involve the incorporation of targeting ligands, stimuli-responsive moieties, or combination therapies to enhance the specificity and efficacy of PLL-ICG nanoparticles for personalized cancer treatment. Overall, the comprehensive understanding gained from this research contributes to the rational design and optimization of PLL-based nanoparticles for advanced biomedical applications, paving the way for the translation of these

innovative nanotherapeutics from the laboratory to the clinic. With continued exploration and refinement, PLL-ICG nanoparticles hold great promise for revolutionizing cancer therapy and addressing unmet clinical needs in the fight against cancer.

6.2 Future scope

The realm of medical biology may benefit greatly from the development of ICG-encapsulated PLL NPs. These NPs have demonstrated a tremendous photothermal effect, which may be verified as a significant advancement in the field of photothermal cancer therapy development. In-vitro cellular photothermal effect is necessary to accomplish this goal. To further verify cellular viability, the MTT assay of cells exposed to an NIR laser can be carried out. This experiment will demonstrate how well ICG works with photothermal therapy. Since several biomarkers are crucial for cell attachment and recognition, ligations of peptides such as arginine-glycine aspartic acid (RGD) can enhance the effectiveness of photothermal therapy to specifically target cancer cells. Targeting folate receptors can be effective in treating breast cancer, the leading cause of mortality for women. Folate receptors are found in many cancer cells. These are the only methods available for actively targeting cancer cells. Their interactions can then be further examined. Further, in-vivo experiments can be done for the targeted drug delivery and photothermal therapy.

References

1. Sathishkumar, K., Chaturvedi, M., Das, P., Stephen, S., & Mathur, P. (2022). Cancer incidence estimates for 2022 & projection for 2025: National Cancer Registry Programme, India. *The Indian journal of medical research*, *156*(4&5), 598–607.
2. *Unequal-toll-of-cancer-on-women 11670349329355, ICMR.*
3. D'Souza, N. D., Murthy, N. S., & Aras, R. Y. (2013). Projection of cancer incident cases for India -till 2026. *Asian Pacific journal of cancer prevention: APJCP*, *14*(7), 4379–4386.
4. Nandakumar, A., Ramnath, T., & Chaturvedi, M. (2009). The magnitude of cancer cervix in India. *The Indian journal of medical research*, *130*(3), 219–221.
5. D'Souza, N. D., Murthy, N. S., & Aras, R. Y. (2013). Projection of burden of cancer mortality for India, 2011-2026. *Asian Pacific journal of cancer prevention: APJCP*, *14*(7), 4387–4392.
6. Arora, R. S., Eden, T. O., & Kapoor, G. (2009). Epidemiology of childhood cancer in India. *Indian journal of cancer*, *46*(4), 264–273.
7. Zhang, P. W., Chen, L., Huang, T., Zhang, N., Kong, X. Y., & Cai, Y. D. (2015). Classifying ten types of major cancers based on reverse phase protein array profiles. *PloS one*, *10*(3), e0123147.
8. Wang, J. J., Lei, K. F., & Han, F. (2018). Tumor microenvironment: recent advances in various cancer treatments. *European review for medical and pharmacological sciences*, *22*(12), 3855–3864.
9. Debela, D. T., Muzazu, S. G., Heraro, K. D., Ndalama, M. T., Mesele, B. W., Haile, D. C., Kitui, S. K., & Manyazewal, T. (2021). New approaches and procedures for cancer treatment: Current perspectives. *SAGE open medicine*, *9*, 20503121211034366.

10. Aboeleneen, S.B., Scully, M.A., Harris, J.C. *et al.* (2022) Membrane-wrapped nanoparticles for photothermal cancer therapy. *Nano Convergence* **9**, 37
11. Kaur, R., Bhardwaj, A., & Gupta, S. (2023). Cancer treatment therapies: traditional to modern approaches to combat cancers. *Molecular biology reports*, *50*(11), 9663–9676.
12. Pérez-Herrero, E., & Fernández-Medarde, A. (2015). Advanced targeted therapies in cancer: Drug nanocarriers, the future of chemotherapy. *European journal of pharmaceutics and biopharmaceutics: official journal of Arbeitsgemeinschaft fur Pharmazeutische Verfahrenstechnik e.V*, *93*, 52–79.
13. Iyer, A. K., Singh, A., Ganta, S., & Amiji, M. M. (2013). Role of integrated cancer nanomedicine in overcoming drug resistance. *Advanced drug delivery reviews*, *65*(13-14), 1784–1802.
14. Yao, Y., Zhou, Y., Liu, L., Xu, Y., Chen, Q., Wang, Y., Wu, S., Deng, Y., Zhang, J., & Shao, A. (2020). Nanoparticle-Based Drug Delivery in Cancer Therapy and Its Role in Overcoming Drug Resistance. *Frontiers in molecular biosciences*, *7*, 193.
15. Agarwal, R., & Kaye, S. B. (2003). Ovarian cancer: strategies for overcoming resistance to chemotherapy. *Nature reviews. Cancer*, *3*(7), 502–516.
16. Yang, D. H., Kim, H. J., Park, K., Kim, J. K., & Chun, H. J. (2018). Preparation of poly-l-lysine-based nanoparticles with pH-sensitive release of curcumin for targeted imaging and therapy of liver cancer in vitro and in vivo. *Drug delivery*, *25*(1), 950–960.
17. Han, G., Wu, S., Wang, J., Geng, X., & Liu, G. (2015). Poly-L-Lysine Mediated Synthesis of Gold Nanoparticles and Biological Effects. *Journal of nanoscience and nanotechnology*, *15*(9), 6503–6508.
18. Jabir, M. S., Taha, A. A., Sahib, U. I., Taqi, Z. J., Al-Shammari, A. M., & Salman, A. S. (2019). Novel of nano delivery system for Linalool loaded on gold nanoparticles conjugated with

CALNN peptide for application in drug uptake and induction of cell death on breast cancer cell line. *Materials science & engineering. C, Materials for biological applications*, *94*, 949–964.

19. Boni, L., David, G., Mangano, A., Dionigi, G., Rausei, S., Spampatti, S., Cassinotti, E., & Fingerhut, A. (2015). Clinical applications of indocyanine green (ICG) enhanced fluorescence in laparoscopic surgery. *Surgical endoscopy*, *29*(7), 2046–2055.
20. Boni, L., David, G., Dionigi, G., Rausei, S., Cassinotti, E., & Fingerhut, A. (2016). Indocyanine green-enhanced fluorescence to assess bowel perfusion during laparoscopic colorectal resection. *Surgical endoscopy*, *30*(7), 2736–2742.
21. Santi, C., Casali, L., Franzini, C., Rollo, A., & Violi, V. (2019). Applications of indocyanine green-enhanced fluorescence in laparoscopic colorectal resections. *Updates in surgery*, *71*(1), 83–88.
22. Zhou, S. C., Tian, Y. T., Wang, X. W., Zhao, C. D., Ma, S., Jiang, J., Li, E. N., Zhou, H. T., Liu, Q., Liang, J. W., Zhou, Z. X., & Wang, X. S. (2019). Application of indocyanine green-enhanced near-infrared fluorescence-guided imaging in laparoscopic lateral pelvic lymph node dissection for middle-low rectal cancer. *World journal of gastroenterology*, *25*(31), 4502–4511.
23. Han, H. S., & Choi, K. Y. (2021). Advances in Nanomaterial-Mediated Photothermal Cancer Therapies: Toward Clinical Applications. *Biomedicines*, *9*(3), 305.
24. Kumari, A., Kumari, K. & Gupta, S. (2019). Protease Responsive Essential Amino-Acid Based Nanocarriers for Near-Infrared Imaging. *Sci Rep* **9**, 20334.
25. Hu, J. J., Cheng, Y. J., & Zhang, X. Z. (2018). Recent advances in nanomaterials for enhanced photothermal therapy of tumors. *Nanoscale*, *10*(48), 22657–22672.

26. Chen, J., Ning, C., Zhou, Z., Yu, P., Zhu, Y., Tan, G., & Mao, C. (2019). Nanomaterials as photothermal therapeutic agents. *Progress in materials science*, *99*, 1–26.
27. Zhao, Y., Chen, B. Q., Kankala, R. K., Wang, S. B., & Chen, A. Z. (2020). Recent Advances in Combination of Copper Chalcogenide-Based Photothermal and Reactive Oxygen Species-Related Therapies. *ACS biomaterials science & engineering*, *6*(9), 4799–4815.
28. Wu, X., Suo, Y., Shi, H., Liu, R., Wu, F., Wang, T., Ma, L., Liu, H., & Cheng, Z. (2020). Deep-Tissue Photothermal Therapy Using Laser Illumination at NIR-IIa Window. *Nano-micro letters*, *12*(1), 38.
29. Chen, M. W., Lu, Q. J., Chen, Y. J., Hou, Y. K., Zou, Y. M., Zhou, Q., Zhang, W. H., Yuan, L. X., & Chen, J. X. (2022). NIR-PTT/ROS-Scavenging/Oxygen-Enriched Synergetic Therapy for Rheumatoid Arthritis by a pH-Responsive Hybrid CeO_2-ZIF-8 Coated with Polydopamine. *ACS biomaterials science & engineering*, *8*(8), 3361–3376.
30. Fu, X., Song, Y., Feng, X., Liu, Z., Gao, W., Song, H., & Zhang, Q. (2024). Synergistic chemotherapy/PTT/oxygen enrichment by multifunctional liposomal polydopamine nanoparticles for rheumatoid arthritis treatment. *Asian journal of pharmaceutical sciences*, *19*(1), 100885.
31. Lu, W., Liu, W., Hu, A., Shen, J., Yi, H., & Cheng, Z. (2023). Combinatorial Polydopamine-Liposome Nanoformulation as an Effective Anti-Breast Cancer Therapy. *International journal of nanomedicine*, *18*, 861–879.
32. Desmettre, T., Devoisselle, J., ophthalmology. (2000), Fluorescence properties and metabolic features of indocyanine green (ICG) as related to angiography. *Elsevier*.
33. Saranath, D., J, A. K.-B. R. (2014), Current status of cancer burden: global and Indian scenario. *researchgate.net*
34. Schroeder, A., Heller, D. (2012), Treating metastatic cancer with nanotechnology. *nature.com*

35. Eckhardt, B., Francis D. (2012), Strategies for the discovery and development of therapies for metastatic breast cancer. *nature.com*
36. Zou, L., Wang, H., He, B., Zeng, L., Tan, T., Cao, H. (2016), Current approaches of photothermal therapy in treating cancer metastasis with nanotherapeutics. *ncbi.nlm.nih.gov*
37. Ferlay, J., Soerjomataram, I., Dikshit, R., Eser, S., Mathers, C., Rebelo, M., Parkin, D. M., Forman, D., and Bray, F. (2015) Cancer incidence and mortality worldwide: Sources, methods and major patterns in GLOBOCAN 2012. *Int. J. Cancer*. 136, E359–E386
38. Tsugane, S., and Sasazuki, S. (2007) Diet and the risk of gastric cancer: review of epidemiological evidence. Gastric Cancer. 10, 75–83
39. Trotti, A., Byhardt, R., Stetz, J., Gwede, C., Corn, B., Fu, K., Gunderson, L., McCormick, B., Morris∫, M., Rich, T., Shipley, W., and Curran, W. (2000) Common toxicity criteria: version 2.0. an improved reference for grading the acute effects of cancer treatment: impact on radiotherapy. *Int. J. Radiat. Oncol.*47, 13–47
40. Miller, A. B., Hoogstraten, B., Staquet, M., and Winkler, A. (1981) Reporting results of cancer treatment. *Cancer.* 47, 207–214
41. Chidambaram, M., Manavalan, R., and Kathiresan, K. (2011) Nanotherapeutics to Overcome Conventional Cancer Chemotherapy Limitations. *J. Pharm. Pharm. Sci*.14, 67
42. Greish, K. (2010) Enhanced Permeability and Retention (EPR) Effect for Anticancer Nanomedicine Drug Targeting, pp. 25–37, *Humana Press*, 10.1007/978-1-60761-609-2_3
43. Maeda, H., Wu, J., Sawa, T., Matsumura, Y., and Hori, K. (2000) Tumor vascular permeability and the EPR effect in macromolecular therapeutics: a review. *J. Control. Release*. 65, 271–284

44. Maeda, H. (2001) SMANCS and polymer-conjugated macromolecular drugs: advantages in cancer chemotherapy. *Adv. Drug Deliv. Rev*.46, 169–85
45. Iyer, A. K., Khaled, G., Fang, J., and Maeda, H. (2006) Exploiting the enhanced permeability and retention effect for tumor targeting. *Drug Discov. Today*. 11, 812–818
46. Matsumura, Y., and Maeda, H. (1986) A new concept for macromolecular therapeutics in cancer chemotherapy: mechanism of tumoritropic accumulation of proteins and the antitumor agent smancs. *Cancer Res.*46, 6387–92
47. Siegel, R. L., Miller, K. D., and Jemal, A. (2018) Cancer statistics, 2018. *CA. Cancer J. Clin*.68, 7–30
48. Gradishar, W. J., Tjulandin, S., Davidson, N., Shaw, H., Desai, N., Bhar, P., Hawkins, M., and O'Shaughnessy, J. (2005) Phase III Trial of Nanoparticle Albumin-Bound Paclitaxel Compared With Polyethylated Castor Oil–Based Paclitaxel in Women With Breast Cancer. *J. Clin. Oncol*.23, 7794–7803
49. Sabbatini, P., Aghajanian, C., Dizon, D., Anderson, S., Dupont, J., Brown, J. V., Peters, W. A., Jacobs, A., Mehdi, A., Rivkin, S., Eisenfeld, A. J., and Spriggs, D. (2004) Phase II Study of CT-2103 in Patients With Recurrent Epithelial Ovarian, Fallopian Tube, or Primary Peritoneal Carcinoma. *J. Clin. Oncol.*22, 4523–4531
50. Bhatt, R., de Vries, P., Tulinsky, J., Bellamy, G., Baker, B., Singer, J. W., and Klein, P. (2003) Synthesis and in Vivo Antitumor Activity of Poly(l -glutamic acid) Conjugates of 20(S)-Camptothecin. *J. Med. Chem*.46, 190–193.
51. Li, C., and Wallace, S. (2008) Polymer-drug conjugates: recent development in clinical oncology. *Adv. Drug Deliv. Rev*.60, 886–98.
52. Seymour, L. W., Ferry, D. R., Anderson, D., Hesslewood, S., Julyan, P. J., Poyner, R., Doran, J., Young, A. M., Burtles, S., Kerr, D. J., and Cancer Research Campaign Phase I/II Clinical Trials committee (2002) Hepatic Drug Targeting: Phase I

Evaluation of Polymer-Bound Doxorubicin. *J. Clin. Oncol*.20, 1668–1676.

53. Batrakova, E., Dorodnych, T., Klinskii, E., Kliushnenkova, E., Shemchukova, O., Goncharova, O., Arjakov, S., Alakhov, V., and Kabanov, A. (1996) Anthracycline antibiotics non-covalently incorporated into the block copolymer micelles: in vivo evaluation of anti-cancer activity. Br. *J. Cancer.* 74, 1545–1552.
54. Choi, H. J., Kim, T. J., Lee, Y. Y., Lee, J. W., Kim, B. G., & Bae, D. S. (2016). Time-lapse imaging of sentinel lymph node using indocyanine green with near-infrared fluorescence imaging in early endometrial cancer. *Journal of gynecologic oncology*, *27*(3), e27.